



Parametrizing the stellar haloes of galaxies

Richard D’Souza,[★] Guinevere Kauffman, Jing Wang and Simona Vegetti

Max Planck Institute for Astrophysics, Karl-Schwarzschild-Str. 1, D-85748 Garching, Germany

Accepted 2014 June 13. Received 2014 June 2; in original form 2014 April 8

ABSTRACT

We study the stellar haloes of galaxies out to 70–100 kpc as a function of stellar mass and galaxy type by stacking aligned *r*- and *g*-band images from a sample of 45 508 galaxies from Sloan Digital Sky Survey Data Release 9 in the redshift range $0.06 \leq z \leq 0.1$ and in the mass range $10^{10.0} M_{\odot} < M_{*} < 10^{11.4} M_{\odot}$. We derive surface brightness profiles to a depth of almost $\mu_r \sim 32 \text{ mag arcsec}^{-2}$. We find that the ellipticity of the stellar halo is a function of galaxy stellar mass and that the haloes of high-concentration galaxies are more elliptical than those of low-concentration galaxies. Where the *g* – *r* colour of the stellar halo can be measured, we find that the stellar light is always bluer than in the main galaxy. The colour of the stellar halo is redder for more massive galaxies. We further demonstrate that the full two-dimensional surface intensity distribution of our galaxy stacks can only be fit through multicomponent Sérsic models. Using the fraction of light in the outer component of the models as a proxy for the fraction of accreted stellar light, we show that this fraction is a function of stellar mass and galaxy type. The fraction of accreted stellar light rises from 30 to 70 per cent and from 2 to 25 per cent for high- and low-concentration galaxies, respectively, over the mass range $10^{10.0} - 10^{11.4} M_{\odot}$.

Key words: Galaxy: formation – Galaxy: halo – Galaxy: structure.

1 INTRODUCTION

Traditionally, galaxies have been studied through their surface brightness profiles (Hubble 1936; de Vaucouleurs 1948). This has not only revealed a wealth of information about their different morphologies but also hints about their formation processes. de Vaucouleurs (1948) first characterized the surface brightness profiles of giant elliptical galaxies as a simple $\log I(R) \propto R^{1/4}$ law, which was later also found to fit the bulges of disc galaxies. On the other hand, the discs of spiral galaxies have been traditionally fitted with exponential profiles (Freeman 1970). Sérsic (1968) showed that all these profiles are specific cases of a more general $\log I(R) \propto R^{1/n}$ function, which fits the surface brightness profile of a large number of galaxies from discs to spheroidals, dwarfs, ellipticals and bulges. The shape of the surface brightness profile provides valuable clues about the way in which different galaxies formed.

As deeper and more resolved surface brightness data became available, deviations from these simple laws became clearly evident, indicating that galaxy formation was a more complex process than previously believed (Kormendy et al. 2009). This discovery motivated the use of multiple components to model the surface brightness profiles of galaxies (Kormendy 1977; Simard et al. 2011; Lackner & Gunn 2012). Bulge–disc decompositions helped distinguish pseudo-bulges ($n \sim 1$) from classical bulges ($n \sim 4$).

Pseudo-bulges are dense central components of disc galaxies that are flattened and rotationally supported and believed to be built out of disc gas. Classical bulges lie on the Fundamental Plane linking galaxy size, luminosity and velocity dispersion (Bender, Burstein & Faber 1992).

With the advent of deeper imaging (through *Hubble Space Telescope* and medium-sized, ground-based telescopes), it has become possible to detect additional fainter stellar structures around both normal galaxies and brightest cluster galaxies (Schweizer 1980; Schweizer & Seitzer 1980; Malin & Carter 1983). Today, stellar haloes of galaxies have been observed and confirmed not only in clusters as intracluster light, but also in a large variety of field galaxies from early-type to late-type spirals. This is consistent with the idea that the faint stellar halo is built up from the debris of smaller galaxies and satellites that are tidally disrupted (e.g. Bullock & Johnston 2005; Cooper et al. 2010).

In the Milky Way and in other nearby disc galaxies, the stellar halo and other tidal features have been directly detected through star counts (Bell et al. 2008; Monachesi et al. 2013; Ibata et al. 2014). Observing the stellar halo through star counts is limited to the Local Universe. The integrated light from deep imaging has enabled studies of the stellar haloes of more distant elliptical and spiral galaxies (see e.g. Mihos et al. 2005; Tal et al. 2009; Martinez-Delgado et al. 2010; van Dokkum, Abraham & Merritt 2014). By using modest aperture telescopes (Martinez-Delgado et al. 2010) with innovative telescope design optimized for low surface brightness emission (van Dokkum et al. 2014), one can reduce the systematic

[★]E-mail: rdsouza@mpa-garching.mpg.de

errors related to flat fielding and the complex point spread function (PSF) of the telescope and reach much deeper limiting depths of $\mu_g \sim 32 \text{ mag arcsec}^{-2}$.

Alternatively, stacking the images of a large number of similar galaxies (e.g. Zibetti, White & Brinkmann 2004; Zibetti et al. 2005; Tal & van Dokkum 2011; Cooper et al. 2013) enables one to study the average stellar haloes of statistical samples of more distant galaxies. The disadvantage is that information on detailed structure is lost. Zibetti et al. (2004) used stacking techniques to study the stellar haloes of edge-on disc galaxies; Tal & van Dokkum (2011) studied the stellar haloes of luminous red galaxies out to $z \sim 0.34$.

Theoretical models (Purcell, Bullock & Zentner 2007; Oser et al. 2010; Lackner et al. 2012; Cooper et al. 2013) predict not only large variations between individual stellar haloes of galaxies, but also systematic variations in the average properties of stellar haloes as a function of certain galaxy parameters (for example, halo mass, stellar mass, galaxy bulge-to-disc ratio, etc.). In order to constrain theoretical models for the formation of stellar haloes, it is important to study the average properties of the surface brightness profiles of galaxies as a function of these galaxy parameters. In this paper, we stack a large number of galaxy images from the Sloan Digital Sky Survey (SDSS) imaging data and study them as a function of stellar mass and galaxy type (late type or early type). Although the SDSS imaging data are relatively shallow, they provide a large number of images with reasonable good quality and consistent calibration, and hence are well suited for stacking to study the faint stellar haloes of galaxies (Zibetti et al. 2004, 2005; Tal & van Dokkum 2011). The systematics of stacking many SDSS images to produce a very deep image have also been well understood and quantified. This is important because studying low-surface brightness structures is highly dependent on a proper estimation and removal of the sky background. We pay particular attention to the residual sky background obtained after stacking the sky-subtracted images from SDSS Data Release 9 (DR9). We then model the surface brightness profile of the stacked galaxy including the stellar halo through multicomponent fits. We then parametrize the contribution of the stellar halo by deriving the fraction of light in the outer component of the galaxy.

In Section 2, we describe how we select and prepare our galaxy images for stacking. In Section 3, we describe in detail the stacking procedure, our error analysis, PSF analysis and the methodology we employ to derive the ellipticity, surface brightness and the colour profiles for each galaxy stack. In Section 4, we present the surface brightness and colour as a function of the stellar mass of the galaxy and of galaxy type. In Section 5, we fit models to these surface brightness profiles and determine the fraction of light in the outer faint stellar component. In Section 6, we summarize and in Section 7, we discuss our results in light of our theoretical understanding of the formation of stellar haloes of galaxies. Throughout this paper, we assume a flat Λ cold dark matter (Λ CDM) cosmology, $\Omega_m = 0.25$, $\Omega_\Lambda = 0.75$ and Hubble parameter $h = 0.73$.

2 SAMPLE SELECTION AND IMAGE PREPARATION

We select isolated central galaxies from the MPA-JHU SDSS spectroscopic ‘value-added’ catalogue in the stellar mass range $10^{10.0} M_\odot < M_* < 10^{11.4} M_\odot$ and in the redshift range $0.06 \leq z$

≤ 0.1 .¹ We apply the isolation criterion outlined in Wang & White (2012): a galaxy of apparent r -band magnitude m_{central} is considered isolated if there are no galaxies in the spectroscopic catalogue at a projected radius $R < 0.5 \text{ Mpc}$ and velocity offset $|\delta z| < 1000 \text{ km s}^{-1}$ with magnitude $m < m_{\text{central}} + 1$, and none within $R < 1 \text{ Mpc}$ and $|\delta z| < 1000 \text{ km s}^{-1}$ with $m < m_{\text{central}}$. We remove all edge-on disc galaxies to avoid adverse PSF effects along the minor axis (de Jong 2008) by choosing only those galaxies with isophotal minor-to-major axis ratio $b/a > 0.3$.

We construct mosaics (1200×1200 pixels) in the g , r and i bands centred on each galaxy using the sky-subtracted SDSS DR9 images and SWARP (Bertin et al. 2002). Galaxies were removed if found unsuitable for stacking. First, galaxy images with a bright source with an r -band Petrosian magnitude greater than 12.0 and within a distance of 1 Mpc from the centre of the galaxy were removed. Secondly, if the masking algorithm (outlined later) failed due to crowded fields, the galaxy image was discarded. Finally, we calculated a histogram of the difference between each galaxy mosaic after masking and transformation (see later) and the stacked image. Galaxy mosaics lying more than 5σ from the mean were discarded. The final sample contains a total of 45 508 galaxies.

For our later analysis, we will stack according to stellar mass and concentration. For the stellar mass stacks, we stack galaxies in stellar mass bins of 0.1 dex. For the highest mass bin, we stack in a bin size of 0.4 dex. Each stack contains both early and late-type galaxies: late-type galaxies dominate the stacks of lower stellar mass whereas early-type galaxies are predominant at high stellar masses. We can parametrize the shape of the galaxy by using the concentration index $C = R_{90}/R_{50}$ (where R_{90} and R_{50} are the radii containing 90 and 50 per cent of the Petrosian r -band luminosity of the galaxy). It has been demonstrated that $C \sim 2.6$ marks the transition from late-type to early-type morphologies (Strateva, Ivezić & Knapp 2001). In order to study the stellar halo separately for late-type and early-type galaxy morphologies, we divide our sample into stellar mass bins of 0.2 dex with a further separation of each stack into high-concentration ($C > 2.6$) and low-concentration galaxies ($C < 2.6$). The number of galaxies in each stack is displayed visually in Fig. 1.

Conservative masking was employed by using multiple runs of SExtractor (Bertin & Arnouts 1996) to create segmentation maps. For this purpose, the mosaics of three bands were stacked together to make a ‘master image’, from which several segmentation masks were created to deal with various types of background and overlapping objects. We used a minimum detection area of 5 pixels, a Gaussian filter for detection and a detection threshold of 1.5σ to create all the masks. For the background detection, we use three variations. We first calculated the mask with a global background. We then calculate the mask with a local background size of 256 pixels with a filter of 20 pixels. Later, we calculated a mask with a smaller background size of 128 pixels with a similar filter size. To deal with extended faint objects, a mask was also created by convolving the master image with an 8×8 pixel top hat kernel before running SExtractor. Each of these masks were successively applied to individual g - and r -band mosaics. The i -band mosaics were only used for creating the master images for the masking procedure.

¹ The stellar masses used here are as defined by the MPA-JHU catalogue (using a methodology similar to that described in Kauffmann et al. 2003a) and corrected for the Hubble parameter $h = 0.73$. The stellar mass estimates in the MPA-JHU catalogue were derived from fits to the SDSS fibre photometry and the total ModelMag photometry.

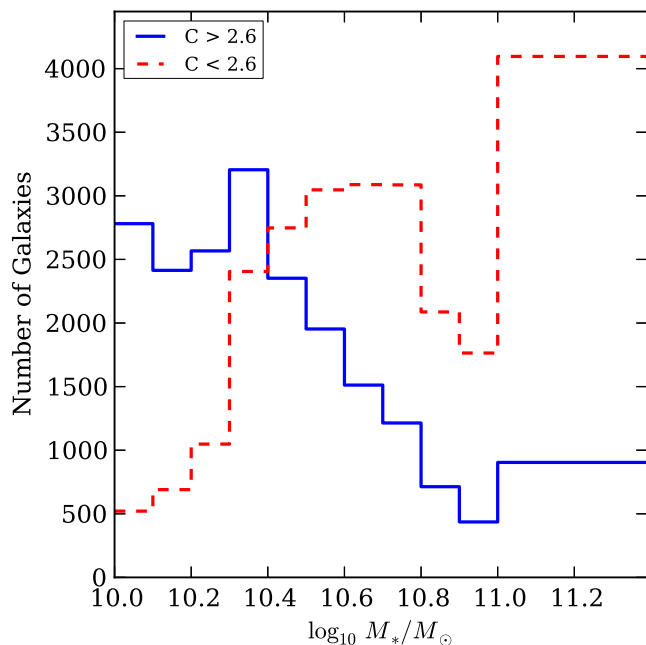


Figure 1. The number of galaxies in each mass bin (0.1 dex in width) split according to low-concentration ($C < 2.6$ blue solid line) and high-concentration ($C > 2.6$ red dashed line) galaxies. The highest mass bin is 0.4 dex in width.

The masked mosaics were then transformed to $z = 0.1$ with the flux-conserving IRAF task GEOTRAN. This involves both a cosmological surface brightness dimming $(1+z)^4$ and an image rescaling. For the final transformed mosaic at $z = 0.1$, 1 pixel = 0.71 kpc. The mosaics were further cropped to a uniform size of 950×950 pixels (550×550 kpc at $z \sim 0.1$) and corrected for Galactic extinction following Schlegel et al. (1998). We ignored K -corrections in scaling the images as they tend to be minimal at $z < 0.1$.

A sizeable number of the final transformed images are oversampled. However, for the redshift range chosen for our sample $z = 0.06-0.1$, this does not significantly affect the noise characteristics of our final transformed images. A final run of SExtractor was used to determine the position angle of the galaxy in the r -band mosaic. This position angle is measured by calculating the second-order moments of the intensity distribution and corresponds to surface brightness threshold $\mu_r \sim 24$ mag arcsec $^{-2}$, or a radius of ~ 10 kpc. Each mosaic was then rotated using GEOTRAN such that the major axis of each galaxy was aligned.

We note that combining galaxy images into mosaics may introduce additional systematics. Blanton et al. (2011) compared the mosaics created from the sky-subtracted images of DR9 and those created directly from the raw images and found that they yield equivalent results.

The sky subtraction in DR9 (Blanton et al. 2011) is a remarkable improvement from early data releases especially for the extended low surface brightness regions around low-redshift galaxies. Blanton et al. (2011) calculate the residual sky background by measuring the mean surface brightness in random patches of size 13×13 native SDSS pixels marked as ‘sky’ in the SDSS pipeline across all imaging runs (see fig. 5 of Blanton et al. 2011). These residuals become significant at depths beyond $\mu_r \sim 26$ mag arcsec $^{-2}$. We will discuss this further in the next section.

3 IMAGE STACKING AND METHODOLOGY

3.1 Stacking procedure

Each stack contains between 1000 and 5000 galaxies with an average of 3000 galaxies. The mosaic images in the g and r bands were stacked using the IRAF task IMCOMBINE, by taking the mean value of each pixel after clipping at the 10th and 90th percentiles.² The images were not weighted in the stacking process so as not to bias the sample. The masked parts of the images were not used when calculating the mean value in IMCOMBINE. To make the stacking computationally easier, the final stacks were built by combining equal stacks of around ~ 100 galaxy images each. By working in narrow mass bin ranges, we avoid the difficult problem of normalizing the size of images in each bin prior to stacking.

3.2 Estimation of background for stacked galaxies

The background ‘sky’ for individual DR9 images consists of the ‘residual’ sky background and light from undetected (unmasked) galaxies. In Appendix A, we quantify the level of light from undetected sources. This tends to be minimal due to the strict masking procedures employed and the fact that we only select isolated galaxies.

To estimate the residual sky background for the stacked image, we calculate the mean intensity in an annulus between 280 and 320 kpc (400–450 pixels) from the centre of the stacked image. We assume that this background is constant over the whole image. To calculate the uncertainty in this background estimation, we calculate the standard deviation of the mean calculated in patches of 16×16 pixels within this annulus.

With the standard SDSS imaging, it is possible to extract radial surface brightness profiles down to $\mu_r \sim 27$ mag arcsec $^{-2}$ (Pohlen & Trujillo 2006). With a better residual background estimation of high signal-to-noise (S/N) stacked DR9 images, it is possible to go significantly deeper. In Fig. 2, we plot the uncertainty in the residual background estimation and the corresponding limiting depth in the r band as a function of the number of co-added objects. The uncertainty in the residual background estimation can be fitted by the function $0.00442/\sqrt{N_{\text{Images}}}$ nanomaggies arcsec $^{-2}$.

3.3 Error estimation

For stacks of a few thousand galaxies, the formal uncertainty in the stacked surface brightness profiles at larger radii is dominated by the uncertainty in subtracting the background sky, which consists of camera noise plus extragalactic background radiation originating in the stellar populations of galaxies at moderate to high redshift. These uncertainties calculated as described in the previous section are depicted as solid error bars in the plots discussed in the next section. In addition to the uncertainty that arises from the sky subtraction, it is interesting to consider the variance that arises from the fact that similar galaxies may have stellar haloes with quite different masses and sizes. This can be quantified for each pixel in our final g - and r -band stacks through a bootstrapping procedure. For each bin, 3000 stacks were created with repetition and the variance in each pixel is calculated for each band. This gives the total uncertainty of each

² Percentile clipping also helps prune any close satellite galaxies which escape the masking procedure.

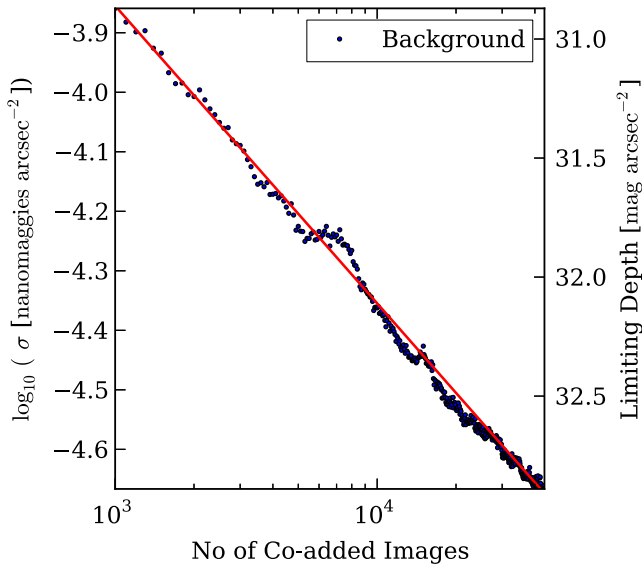


Figure 2. The logarithm of the uncertainty in background removal as a function of the number of co-added images. The right-hand axis depicts the limiting surface brightness depth. The red line indicates the function $0.00442/\sqrt{N_{\text{Images}}}$ nanomaggies arcsec $^{-2}$.

pixel. After accounting for the formal uncertainty, the variance in the surface brightness profiles can be calculated. The shaded regions in the plot depict the standard error in the mean due to the variance in the shape of the profile.

To verify that the faint outer stellar halo visible in our stacks between 30 and 32 mag arcsec $^{-2}$ is not a product of systematics in the data or due to our stacking procedure, we created equivalent background stacks (nearly 3000 images) for each bin by choosing a location 5 Mpc away from the centre of the galaxy in a random direction where no large galaxies were found within a distance of 1×1 Mpc. We found that evaluating the background at these very large distances made no difference to our results.

3.4 PSF effects

The PSF flattens the ellipticity and the surface brightness profiles at the centre of the galaxy at radii less than ~ 10 kpc. For deep images, the light in the faint outskirts of the stack can be dominated by the scattered light from the centre of the galaxy. Failure to account for the difference in the extended wings of the PSF, especially in the i band, can lead to a reddening of the colour of the stellar halo (de Jong 2008). This is very visible along the minor axis of edge-on disc galaxies where the surface brightness decreases faster than the profile of the wings of the PSF.

We choose not to deconvolve the stacked galaxy profiles. The effect of the PSF is much smaller in our work than that of Tal & van Dokkum (2011) due to the fact that the galaxies are much closer in redshift. For data interpretation purposes, we will model the two-dimensional stacked image of the galaxy convolved with the average PSF. We have thus constructed average PSF stacks in the g , r and i bands by combining the synthetic PSFs created using Robert Lupton's Read Atlas Images code³ and stacked bright star images according to the procedure outlined in Tal & van Dokkum (2011). The PSF profiles for the g , r and i bands are shown in Fig. 3.

³ http://www.sdss.org/DR7/products/images/read_psf.html

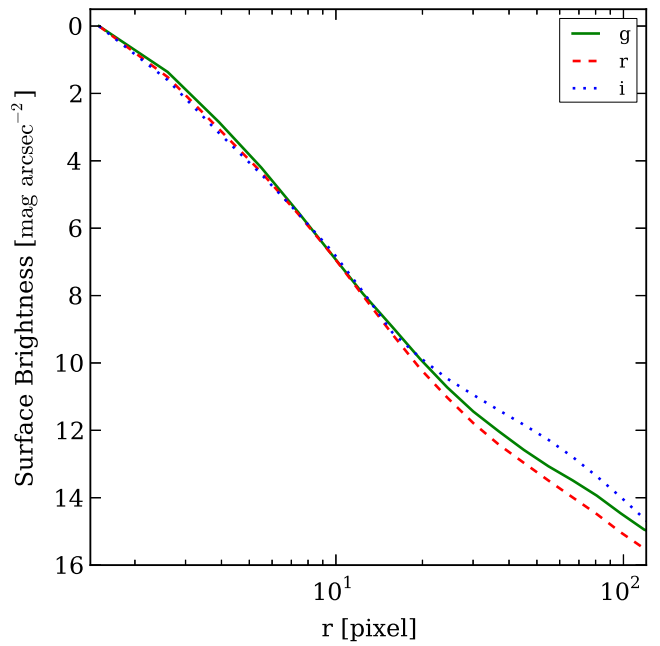


Figure 3. SDSS PSFs colour coded for the g , r and i bands as indicated by the legend.

Due to the fact that the PSFs in the g and in the r bands are similar (see also fig. 2 of de Jong 2008 as well as fig. 6 of Bergvall, Zackrisson & Caldwell 2010), our $g - r$ colour profiles are not significantly affected by PSF effects, especially in the outer parts of the profiles. We investigate this further in Appendix C. However, the i -band PSF does differ significantly (see Fig. 3) in having wings that extend to much larger distances. We therefore avoid the use of the SDSS i band.

3.5 Ellipticity, surface brightness and colour profiles

Measuring the ellipticity can help quantify the shape of the average stellar halo. The standard ELLIPSE task from the STSDAS package in IRAF performs poorly at low S/N regions especially in the outer parts of the stellar halo. For this reason, the ellipticity profiles ($1 - b/a$) for each of the aligned galaxy stacks are determined by generating intensity contours at various distances from the centre of the stacked image of the galaxies in the r band after appropriate smoothing. For deriving contours which were greater than 20 pixels away from the centre of the galaxy stack, we smooth the image with a Gaussian filter with a width of 3 pixels. For contours beyond 60 pixels from the centre of the galaxy stack, we smooth the image with a larger Gaussian filter (width of 5 pixels).

In Fig. 4, we plot ellipticity profiles out to radii of 30–50 kpc for our stacks divided according to stellar mass and concentration. Information on the shape of stellar haloes can be inferred from the average ellipticity profiles for each stack. Only the inner part (< 10 kpc) of the ellipticity profile is significantly affected by the PSF. The outer parts of the ellipticity profile show a gradual change in ellipticity with radius. The ellipticity profile of the stacks of lower stellar mass decreases as the radius increases, i.e. for these galaxies the outer part of the stellar halo is more circular than the inner part of the galaxy. The ellipticity of the outer part of the stellar halo increases as a function of M_* . The highest stellar mass bins have a maximum outer ellipticity of ~ 0.17 , which remains approximately constant from 30 to 50 kpc.

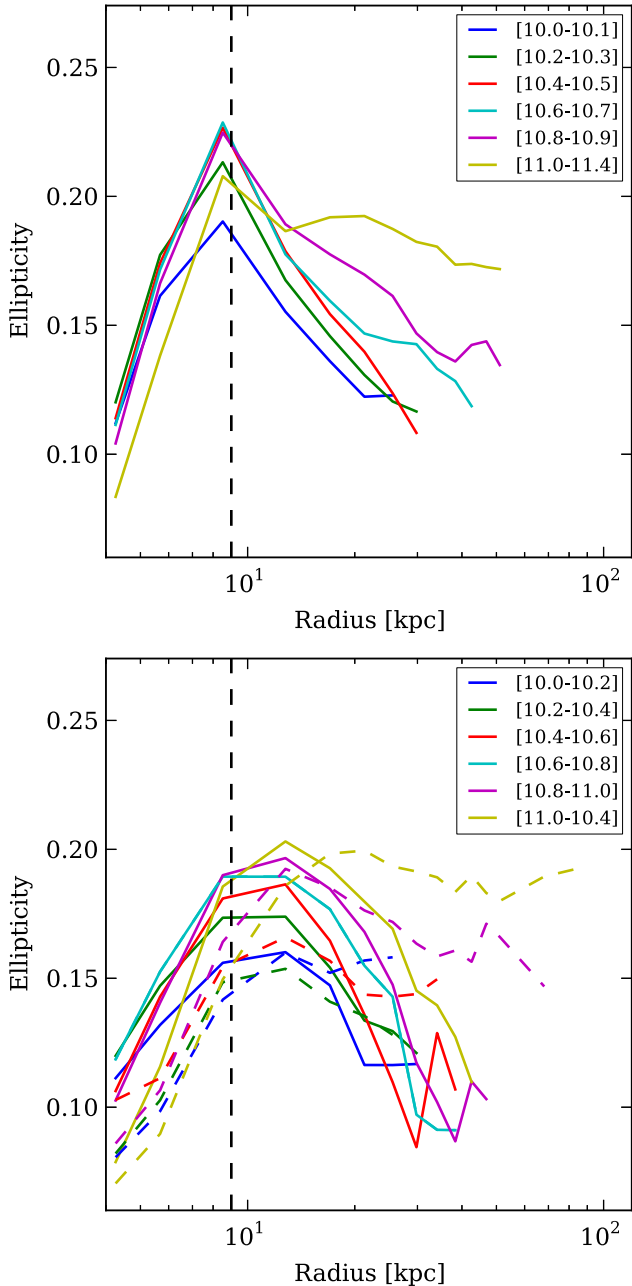


Figure 4. (a) Ellipticity profiles for successive stellar mass bins. (b) Ellipticity profiles for each of the stellar mass bins divided according to concentration. Solid lines and dashed lines indicated low ($C < 2.6$) and high ($C > 2.6$) concentration galaxies, respectively. The vertical dashed line indicates the maximum radius affected by the PSF.

In Fig. 5, we show the stacked image of high-concentration galaxies stacked in the mass range $10^{11.0} M_{\odot} < M_{*} < 10^{11.4} M_{\odot}$ along with elliptical contours drawn at various radii.

We find that the stellar haloes of low-concentration galaxies tend to be spherical, while the stellar haloes of high-concentration galaxies tend to be elliptical. The peak in the ellipticity profiles of low-concentration galaxies at ~ 15 kpc may be due to the combined effect of stacking disc galaxies at varying inclinations. At fixed mass, the ellipticity of the highest stellar mass, high-concentration galaxies reaches values of 0.2 and is approximately constant from 20 to 100 kpc. By contrast, the measured ellipticity ($1 - b/a$) of low-concentration galaxies is around 0.1.

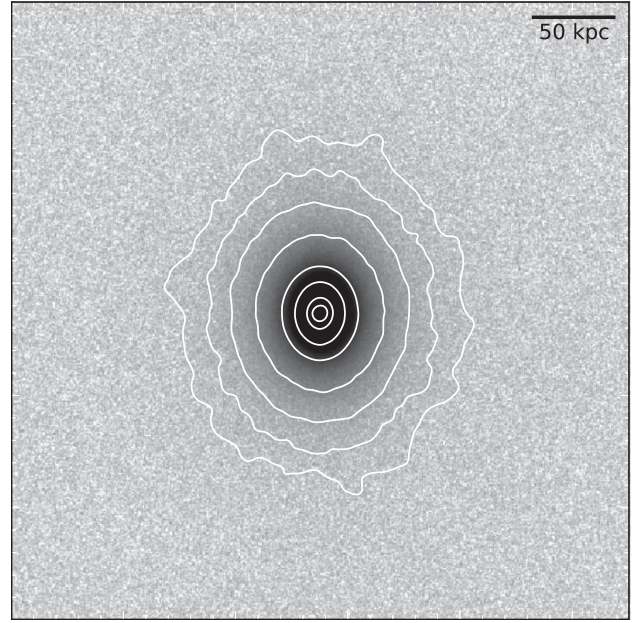


Figure 5. The stacked image consisting of 4040 images in the mass range $10^{11.0} M_{\odot} < M_{*} < 10^{11.4} M_{\odot}$ and $C > 2.6$. Elliptical contours are drawn at 5, 10, 20, 30, 50, 70, 90 and 110 kpc.

Are these results consistent with other measurements? The stellar halo of M31 can easily be measured out to large distances and is found to be nearly spherical (Ibata et al. 2014). At 80 kpc for high-concentration high stellar mass galaxies, the measured ellipticity is 0.21 ± 0.08 . This is also consistent with the ellipticity of the stellar halo of LRGs measured by Tal & van Dokkum (2011) which lies around ~ 0.25 – 0.3 . On the other hand, Sesar, Jurić & Ivezić (2011) measured the axial ratio of the Milky Way stellar halo out to a distance of 35 kpc and estimated it as $q \sim 0.7$, i.e. an ellipticity of 0.3, which lies outside the range spanned by our estimates. This may imply that the Milky Way’s halo is unusual. Huang et al. (2013) have also found that the outer parts of nearby elliptical galaxies is higher than the inner parts of the galaxy.

We note, however, that when stacking aligned galaxies together, we assume that the outer stellar halo is also aligned with the shape of the galaxy. If this were not the case, it would lead to a systematic uncertainty in the intrinsic ellipticity which would increase with radius. As a result, the ellipticity measured is a lower limit on the true average intrinsic ellipticities of the stellar haloes of the galaxies which make up the stack. Convolution of the stacked images creates additional measurement uncertainties.

Using these ellipticity profiles, we derive surface brightness in the r -band and $g - r$ colour profiles in elliptical annuli after background subtraction.

At radii where the ellipticity estimates are no longer reliable, we assume that the ellipticity profile flattens out at the furthestmost determined value of the ellipticity.

4 ANALYSIS OF STACKED IMAGES

4.1 Profiles in stellar mass bins

In Fig. 6, we show the average surface brightness profiles and the average $g - r$ colour profiles for our galaxy stacks in stellar mass bins. The surface brightness profiles extend reliably to a depth of $\mu_r \sim 32$ mag arcsec⁻². The profiles of highest mass bins

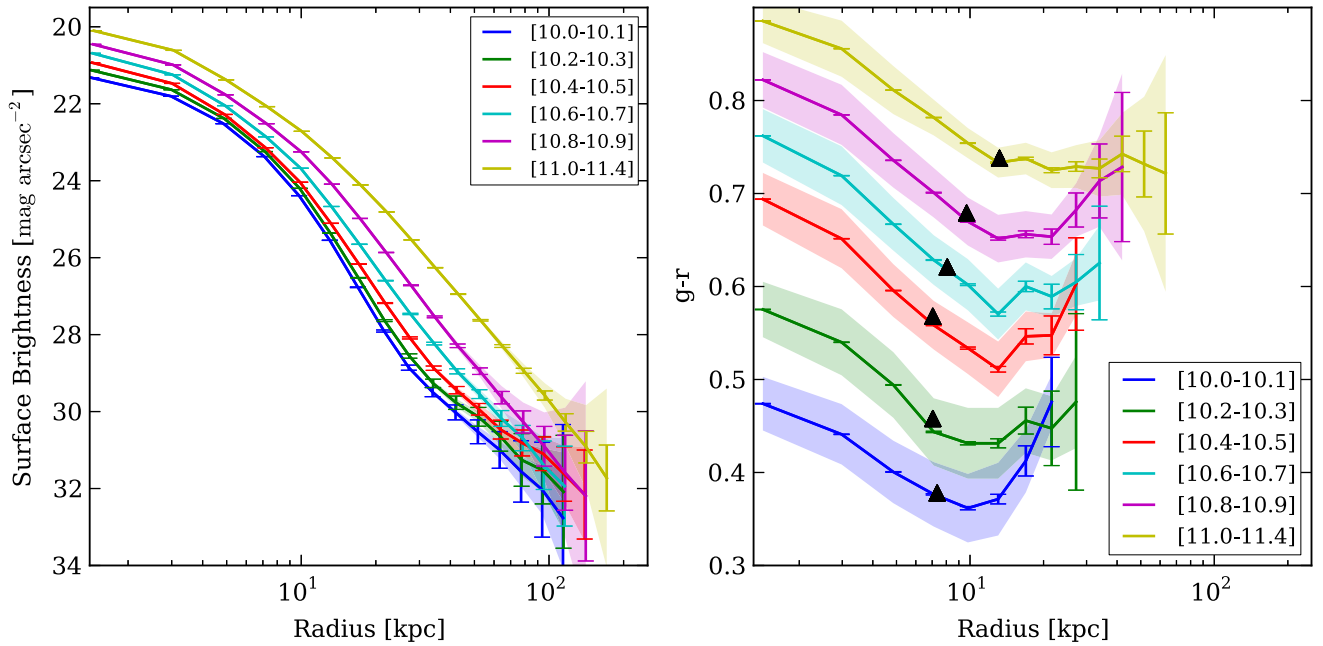


Figure 6. Surface brightness profiles and $g-r$ colour profiles of stacks for successive stellar mass bins. The error bars show the standard error of the mean which includes the instrumental errors and uncertainty in background subtraction, while the shaded regions show the standard error of the mean due to the variation in the shape of the stellar halo. The triangles in the colour profiles mark the average $R50$ of galaxies in the respective bin.

reach out to 100–150 kpc, while the lower mass bins extend up to 60–100 kpc. The surface brightness profile of the stellar halo show variations with stellar mass. As discussed in Cooper et al. (2013), the trend in the surface brightness profiles in the stellar mass range $10^{10.7} M_{\odot} < M_{*} < 10^{11.4} M_{\odot}$ is consistent with the theoretical predictions. In this paper, we extend the analysis down to $10^{10} M_{\odot}$; comparison with model predictions will form the subject of a future paper.

The triangle markers in the colour profiles indicate the average $R50$ (the radius enclosing 50 per cent of the Petrosian r -band luminosity of the galaxy) for each mass bin. For each mass bin, there is a flattening in the colour profile and a hint of an upturn beyond the average $R50$ indicating that we may be seeing the effects of an older accreted component. We will quantify this in more detail in the next section.

4.2 Profiles in stellar mass bins divided by concentration

In Fig. 7, we show the average surface brightness profile and the average $g-r$ colour profiles for our galaxy stacks separated into high ($C > 2.6$) and low ($C < 2.6$) concentration galaxies.

The surface brightness profiles reveal a clear difference in the shapes of the stellar haloes of high-concentration and low-concentration galaxies. We can parametrize the shape of the stellar halo by measuring its outer slope. The outer slope is measured through a Bayesian methodology that takes into consideration the scatter due to the variance of the shape of the surface brightness profile of the galaxy. The details are outlined in Appendix B.

In Fig. 8, we plot the slope $\Gamma = d(\log_{10} I)/d(\log_{10} R)$ beyond 25 kpc of the surface brightness profile as a function of stellar mass and galaxy type. At these radii, the surface brightness profiles are not significantly affected by the PSF. The error bars include the variance of the shape of the surface brightness profile of the galaxies in the stack estimated through bootstrapping. For low-concentration galaxies, the outer slope steepens from $\Gamma \sim -2.5$ at low stellar

masses to $\Gamma \sim -4.4$ at higher stellar masses. For high-concentration galaxies, the outer slope steepens from $\Gamma \sim -2.3$ at low stellar masses to $\Gamma \sim -3$ at higher stellar masses. At fixed mass, the outer slopes of the profiles of low-concentration galaxies are steeper than those of high-concentration galaxies. The variance in the slope is much larger for low-concentration than high-concentration galaxies. Similarly, the variance in the slope is much larger for low-mass than high-mass galaxies.

Ibata et al. (2014) analyse the power-law slope of the two-dimensional projected distribution of star counts in M31 and find $\Gamma = -2.30 \pm 0.02$. We again caution the reader that in stacking large number of galaxies together with different concentrations, the resulting outer slope is a linear combination of the outer slopes of the individual galaxies which go into the stack, so our results are not directly comparable to those obtained for individual galaxies.

4.3 Colour profiles as a function of stellar mass and concentration

The $g-r$ colour profiles extend out to 15–35 kpc for low-concentration galaxies and up to 40–70 kpc for high-concentration galaxies. There also appears to be a clear separation between the inner ($R < 10$ kpc) colour profiles, where $g-r$ decreases as a function of radius, to a region where colour remains more constant. This is seen for both low- and high-concentration galaxies. Low-concentration galaxies show steeper inner colour gradients than high-concentration galaxies. The colour gradient is also steeper in low-concentration galaxies with high stellar masses than in low-concentration galaxies with low masses (see also Suh et al. 2010; Tortora et al. 2010; Gonzalez-Perez, Castander & Kauffmann 2011).

For low-concentration galaxies, there appears to be a minimum in the $g-r$ colour beyond which the colour profiles redden. This minimum occurs between 10 kpc for low-mass galaxies and 20 kpc for higher mass systems. For high-concentration galaxies, the colour

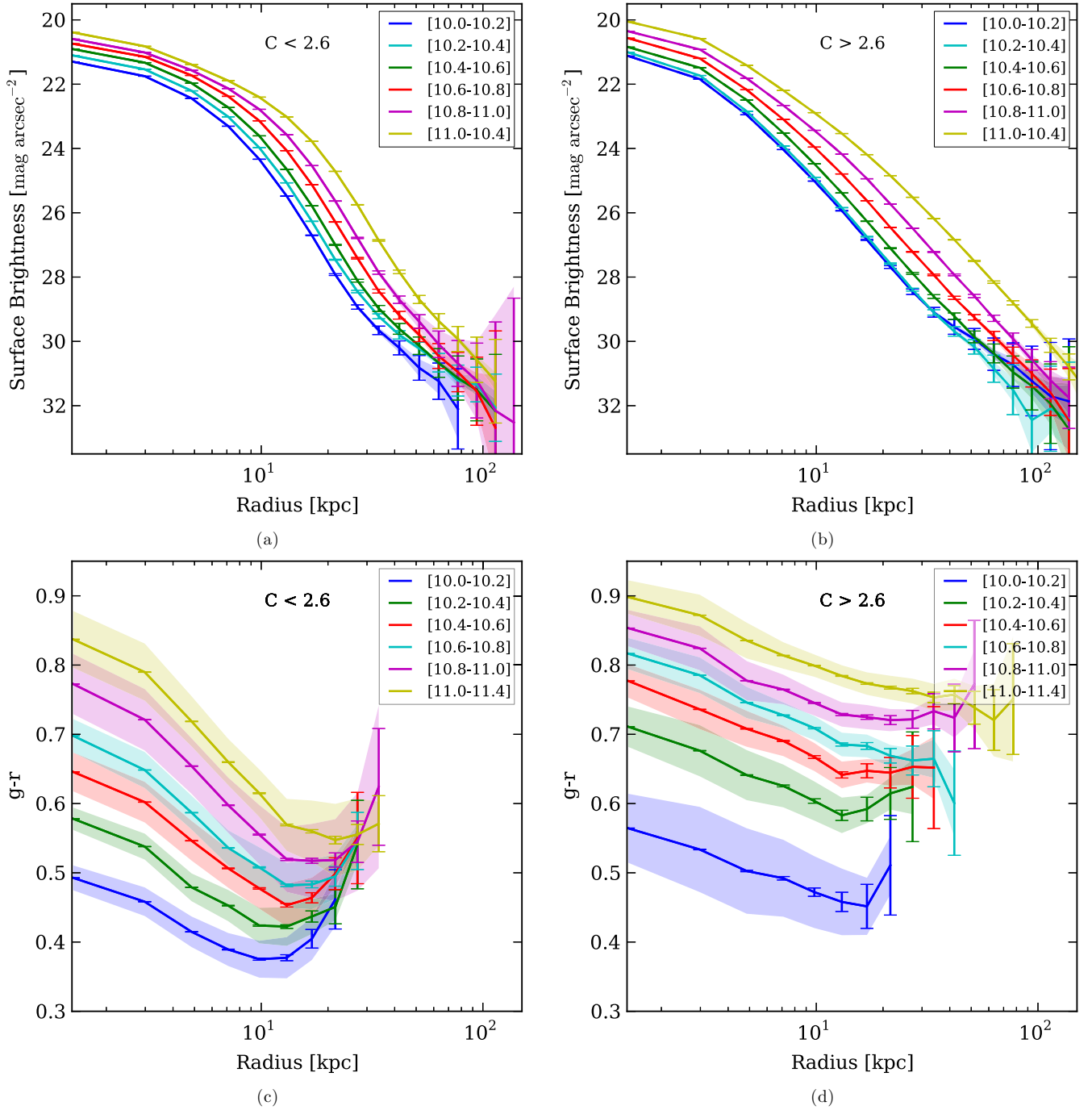


Figure 7. Surface brightness and $g-r$ colour profiles of the stellar mass bins divided according to concentration. The error bars show the standard error of the mean which includes the instrumental errors and the uncertainty in background subtraction, while the shaded regions show the standard error in the mean due to the variation in the shape of the stellar halo.

profiles flatten, but do not exhibit a pronounced upturn. This is consistent with the flattening in colour profiles detected in LRGs (Tal & van Dokkum 2011). Reddening of the colour profile at large radii cannot be attributed either to the difference in the PSF in the g and r bands or due to the errors in the background subtraction. We investigate this further in Appendix C.

La Barbera et al. (2012) have derived median-stacked colour profiles of early-type galaxies from SDSS. In particular, their $g-r$ colour profile can be directly compared to our $g-r$ colour profile

for high-mass high-concentration galaxies. Both the colour profiles are consistent with each other within error bars. In particular, there is excellent agreement in the outer part. Our $g-r$ colour profiles are redder by 0.05 mag at the centre of the galaxy stack. This can be attributed to the effect of the PSF at the centre of the galaxy stack (see Appendix C).

The colour profiles of low-concentration galaxies do not probe the area where the stellar halo becomes dominant. Bakos, Trujillo & Pohlen (2008) have shown that 90 per cent of the light profiles

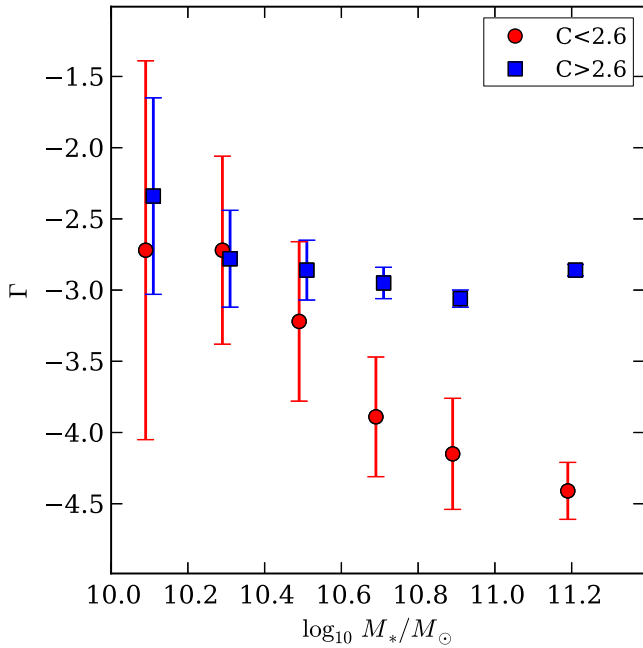


Figure 8. The slope $\Gamma = d(\log_{10} I)/d(\log_{10} R)$ of the surface brightness profile beyond 25 kpc. Blue represents high-concentration galaxies, while red represents low-concentration galaxies. The errors represent the total variance in the slope of the surface brightness profile estimated from bootstrapping the samples in the stack.

of the discs of late-type galaxies exhibit deviations from a pure exponential either as truncations (60 per cent) or as antitruncations (30 per cent). The colour profiles of discs with truncations are ‘U-shaped’. Discs with antitruncations exhibit a plateau in $g - r$ colour at large radii. When stacking a large number of low-concentration galaxies together containing with a minimum or a flattening in the $g - r$ colour profile, the combined effect results in behaviour intermediate between the two. Deeper data are required to probe the colours of stellar populations in the stellar halo. Monachesi et al. (2013) detect a flattening of the colour profile of the stellar halo of M81.

The presence of bluer colours in the outer end of both low- and high-concentration galaxies as compared to the centre of the galaxy may indicate the presence of stars with significantly younger populations in these outer parts. However, it will be difficult to confirm this without being able to break the degeneracy between age and metallicity by using colours that involve either the i or z bands.

We plot the $g - r$ colour gradient $\nabla_{g-r} = \frac{\Delta(g-r)}{\Delta(\log R)}$ for our galaxy stacks in Fig. 9. For low-concentration galaxies, we evaluate the slope for the path of the steepest descent interior to the minimum in the $g - r$ colour profile. For high-concentration galaxies, the slope is derived for the steepest descent interior to the point where the $g - r$ colour profile flattens. Since the colour profile is affected by the PSF at the centre of the galaxy stack, the analysis is restricted to radii beyond 3 kpc. The gradient is first evaluated from 3 kpc right up to the minimum in the $g - r$ colour profile, and the path length over which the gradient is calculated is decreased step-by-step until the gradient reaches its maximum. Fig. 9 shows that colour gradients are stronger in late-type galaxies than in early-type galaxies. In early-type galaxies, the gradients do not depend on stellar mass, but in late-type galaxies, high-mass galaxies have much steeper gradients than low-mass galaxies.

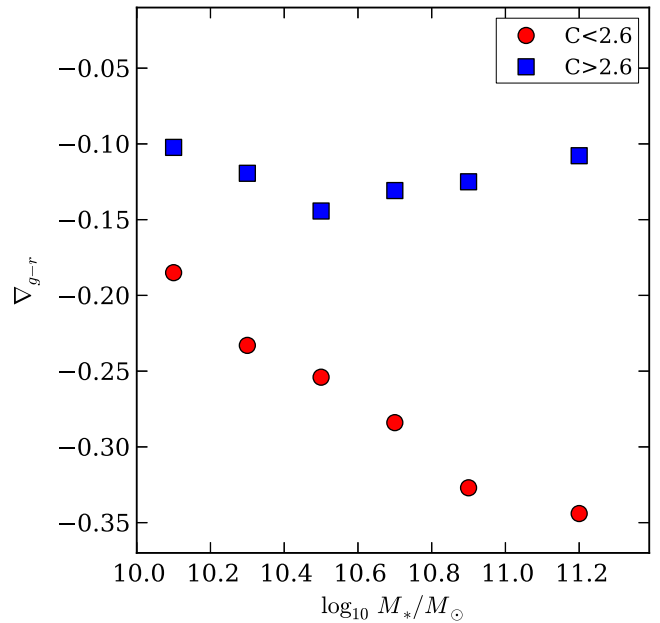


Figure 9. The gradient in the $g - r$ colour profile, $\nabla_{g-r} = \frac{\Delta(g-r)}{\Delta(\log_{10} R)}$, measured along the path of the steepest descent for low-concentration galaxies interior to the radius where the profile exhibits an upturn, and for high-concentration galaxies interior radius where the colour profile flattens.

5 MULTICOMPONENT MODELLING OF THE GALAXY STACKS

For each stacked image, we model the full two dimensional r -band intensity distribution of the galaxy stack using multicomponent Sérsic models. We are particularly interested in modelling the outer stellar halo light of the galaxy and in placing constraints on the amount of accreted stellar material. We are confident that the depth of our stacked images means that we can reach out into the extended stellar halo of the galaxy. Theoretical considerations indicate that there should be an inflexion or a change in the surface brightness profile of the galaxy where the accreted stellar component begins to dominate (Cooper et al. 2013).

The Sérsic (1968) profile $\log I(r) \propto r^{1/n}$ is the most versatile among the models and is traditionally used to fit the surface brightness profile of galaxies. The Sérsic profile reduces to an exponential ($n = 1$) profile for disc galaxies, while $n = 4$ profiles (de Vaucouleurs 1948) has been used to model bulges and ellipticals. Kormendy et al. (2009) have demonstrated that the Sérsic profile fits elliptical galaxies and spheroidals very well over a large dynamic range in radius. They also suggested that departures from these profiles could provide new insights into galaxy formation. In this paper, we leave aside the issue of departures from the Sérsic profile at small radii in our galaxy stacks. Our aim is to explore our ansatz that the excess light (deviations from the single-Sérsic profile) detected at large radii ($R > 20$ kpc) is indicative of additional components in the galaxy, which may be attributed to accreted stellar material. Our second ansatz is that the radial variation of ellipticity can also be indicative of various galaxy formation processes. In particular, the difference in ellipticity between the inner part of the galaxy and the outer stellar halo of the galaxy may yield clues to the origin of these components.

Deviations from simple profiles at large radii and the radial variation in ellipticity can be adequately modelled through

multicomponent modelling, where each component can be represented by a Sérsic profile with a fixed ellipticity. The flexibility of the Sérsic profile helps us model a large variety of possible profiles. The real challenge of modelling galaxies is in assigning a physical significance to each of these components. In fitting multiple components to our galaxy stacks, we are motivated by the results of Cooper et al. (2013) who have demonstrated theoretically from particle-tagging methods that the *in situ* and the accreted surface density profiles are well fitted by Sérsic (1968) functions, while the total profile is best fitted by a sum of these two functions.

Such an approach have been attempted previously for nearby galaxies. In particular, Huang et al. (2013) and Mosleh, Williams & Franx (2013) have recently showed for nearby galaxies that multi-component Sérsic models are needed to model the two-dimensional intensity distribution of galaxies. Huang et al. (2013) decomposed nearby elliptical galaxies into three sub-components: a compact ($R_e < 1$ kpc) inner component, an intermediate-scale ($R_e \sim 2.5$ kpc) middle component, and a dominant extended ($R_e \sim 10$ kpc) outer envelope.

We seek to model the two-dimensional intensity profile of the galaxy with a minimum number of components through a Bayesian technique following Yoon, Weinberg & Katz (2011). In the following sub-sections, we model separately the stacks of high-concentration and low-concentration galaxies. We first show that a single component is not sufficient to model the surface brightness profile of high-concentration galaxies. We demonstrate how the surface brightness profile of high-concentration galaxies can be successfully modelled by two components. For low-concentration galaxies, we show that we may need three components to model the disc breaks of galaxies in addition to the stellar halo. For all our fitting procedures, we use the full two-dimensional information in the stacked image. We also test our modelling on mock images of high- and low-concentration galaxies.

5.1 High-concentration galaxy stacks

High-concentration galaxies are simpler to model than low-concentration galaxies. Motivated by this, we first fit a single two-dimensional Sérsic model with a fixed ellipticity to our high-concentration galaxy stack:

$$I(R) = I_e \exp \left\{ -b_n \left(\left(\frac{R(q)}{R_e} \right)^{1/n} - 1 \right) \right\}, \quad (1)$$

where I_e is the intensity at the effective radius R_e that encloses half of the total light from the model and n is the Sérsic index. The constant b_n is defined in terms of the Sérsic index. The radial distance, R , is a function of the Cartesian coordinates and the ellipticity q of the model. We also model an additional constant sky component. A single-Sérsic model so defined has a total of four free parameters.

We compare this with a double-Sérsic model with a common centre and with different ellipticities for each Sérsic component. Sérsic profiles extend out to infinity. In order to ensure that the outer stellar halo is determined by only one component, we smoothly cut off the inner Sérsic profile at large radii: the surface brightness profile is suppressed beyond $7 R_e$ and drops to zero outside $8 R_e$.⁴ With an additional constant sky component (c), the double-Sérsic model has a total of nine free parameters. There are two additional

Table 1. Parameters of the double-Sérsic model.

Double Sérsic	
$n1$	Inner Sérsic index
$r1$	Inner effective radius
$i1$	Inner effective intensity
$q1$	Inner ellipticity
c	Residual sky value
$n2$	Outer Sérsic index
$r2$	Outer effective radius
$i2$	Outer effective intensity
$q2$	Outer ellipticity

free parameters for the centre of each model. To reduce the number of free parameters, we determine and fix the centre of the galaxy stack by fitting a single-Sérsic model with variable parameters for the centre. All the models considered are symmetric along the major axis and the minor axis. The asymmetries in the image (in the form of bars, bulges, discs, pseudo-bulges, etc.) are not explicitly modelled and appear as residuals. The parameters of the double-Sérsic model are summarized in Table 1.

For the fitting procedure, each model was convolved with the average stacked SDSS PSF before fitting (see Section 3.4). We employ a Bayesian technique with uniform and physical priors for all the parameters θ (I_e : 0–1 nanomaggies arcsec⁻²; R_e : 1–100 pixels; n : 0–10; c : 0–1 nanomaggies arcsec⁻²; q : 0–10).

Applying Bayes' theorem, we can find the posterior probability distribution over the parameters θ as

$$p(\theta | \mathbf{D}) = \frac{p(\mathbf{D} | \theta)}{\int_{\theta} p(\mathbf{D} | \theta) p(\theta) d\theta} \cdot p(\theta), \quad (2)$$

where $\int_{\theta} p(\mathbf{D} | \theta) p(\theta) d\theta$ is the model evidence and \mathbf{D} is the data. $p(\mathbf{D} | \theta)$ is the likelihood which can be constructed as follows:

$$\log(L) = -\frac{1}{2} \log((2\pi)^k \Sigma) - \frac{1}{2} (\mathbf{D} - \mu(\theta))^T \Sigma^{-1} (\mathbf{D} - \mu(\theta)), \quad (3)$$

where Σ is the covariance matrix (which is diagonal in this case), \mathbf{D} is the stacked data, μ is the model as a function of the parameters θ and k is the number of independent pixels.

We use MULTINEST (Feroz, Hobson & Bridges 2008; Feroz et al. 2013), a Bayesian inference tool on the full stacked image. This has the advantage over GALFIT (Peng et al. 2010) in that it can explore the complete parameter space. We use the full image 950×950 pixels for the fitting procedure. This is essential for a proper determination of the residual sky component in the stacked images. In general, the determination of the outer Sérsic index is correlated with the sky component.

We generate a full posterior probability distribution function (PDF) of all the parameters using MULTINEST. This allows us to evaluate the degeneracies in the parameters. If the posterior PDF is double modal (i.e. contains two maxima), we choose the most physical model such that the effective intensity (I_e)/effective radius (R_e) of the innermost component should be larger/smaller than that of the outer component. For the final parameters of the model, we use the mean values of the posterior PDF. These mean values automatically encode information on the parameter degeneracies.

To compare the various models with each other, we can use two approaches. The first involves using the Bayesian 'evidence' marginalized over the model parameters for model comparison. This compares models on a global scale. On the other hand,

⁴ The same procedure is followed in SDSS for pure de Vaucouleurs profile to calculate ModelMag.

Table 2. We compare the double-Sérsic model with the single-Sérsic model by comparing $2 \log_e(B_{D/S})$, where $B_{D/S}$ is the Bayes factor favouring the double-Sérsic model over the single-Sérsic model.

Mass bin	$2 \log_e(B_{D/S})$
10.0–10.2	3713
10.2–10.4	9779
10.4–10.6	23 508
10.6–10.8	30 831
10.8–11.0	21 730
11.0–11.4	18 727

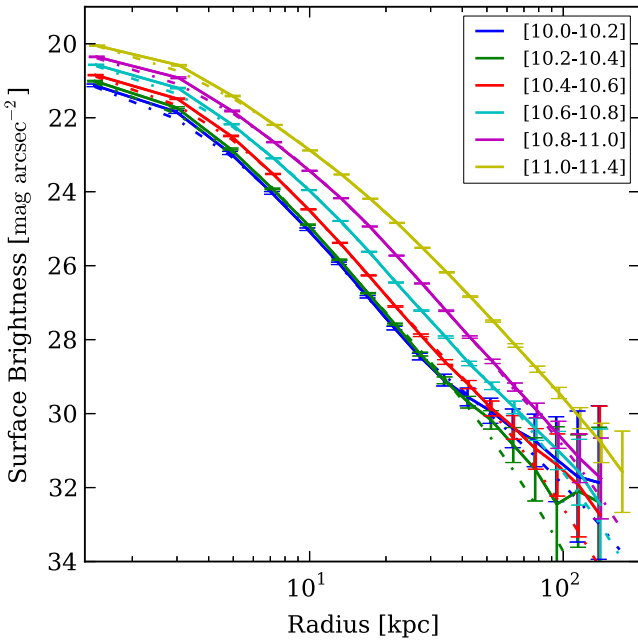


Figure 10. We compare the surface brightness profiles of the high-concentration galaxy stacks with their corresponding double-Sérsic models.

comparing residuals (or the reduced chi-square) in specific regions of the stacked image allows one to judge the goodness of fit for specific components of the galaxy stack including the stellar halo.

To compare models globally, we construct the Bayes factor (B_{10} – hypothesis 1 over hypothesis 0). Kass & Raftery (1995, Journal of American Statistical Association) suggest comparing $2\log_e(B_{10})$ and note that a factor > 10 is indicative of strong evidence against hypothesis 0. The square root of $2\log_e(B_{10})$ gives us the level of significance between the two models. We compare the factor $2 \log_e(B_{D/S})$ which is comparing the double-Sérsic model over the single-Sérsic model for a range of mass bins in Table 2. In Fig. 10, we show how well the double-Sérsic model fits the surface brightness profiles for a range of stellar mass bins.

In Fig. 11, we compare the single-Sérsic and double-Sérsic models for the high-concentration galaxy stack in the highest stellar mass bin $10^{11.0} M_\odot < M_* < 10^{11.4} M_\odot$. The single-Sérsic function fits the symmetric central high S/N part of the surface brightness profile up to a surface brightness of $\mu_r \sim 27 \text{ mag arcsec}^{-2}$ reach-

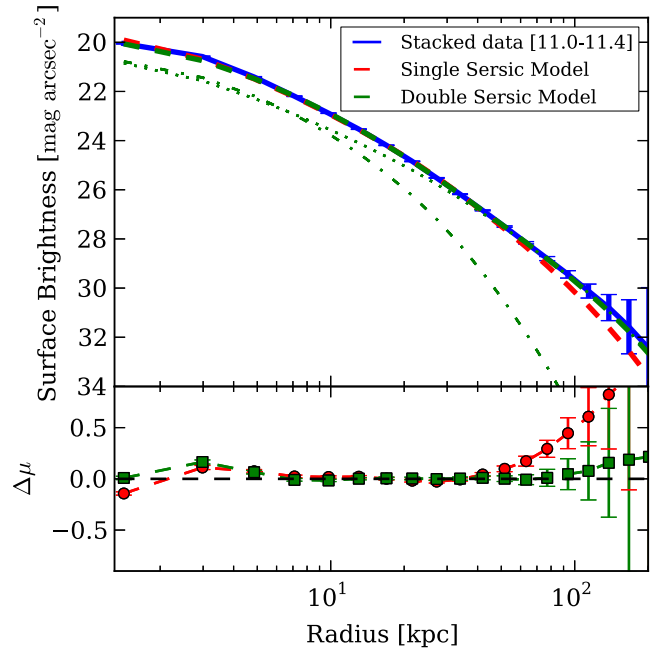


Figure 11. Comparison of the double-Sérsic (dashed green) and the single-Sérsic (dashed red) models with the surface brightness profile of the high-concentration highest stellar mass bin stack $C > 2.6, 10^{11.0} M_\odot < M_* < 10^{11.4} M_\odot$. For the double-Sérsic model, the internal component is denoted by the dot-dashed line while the outer component is denoted by the dotted line.

ing out to 30 kpc. Note that all internal galaxy components (e.g. bulges, discs, pseudo-bulges) are averaged out and incorporated into the single-Sérsic fit. Beyond 30 kpc, excess light is detected. The double-Sérsic profile on the other hand provides an excellent fit up to a depth of $\mu_r \sim 32 \text{ mag arcsec}^{-2}$ reaching out to 130 kpc. The residuals are shown in the panel below in Fig. 11. The residuals of the double Sérsic are less than $0.2 \text{ mag arcsec}^{-2}$ across the whole radial range (0–120 kpc) of the galaxy stack. The residuals at the centre are attributed to the asymmetric part of the intensity distribution at centre of the galaxy stack due to the various internal galaxy components mentioned above. The PDFs and the correlations between the various parameters of the double-Sérsic model for the high-concentration highest stellar mass bin stack ($C > 2.6, 10^{11.0} M_\odot < M_* < 10^{11.4} M_\odot$) are shown in Fig. 12.

We find that the double-Sérsic profile provides a much better fit for all high-concentration galaxies across all mass bin ranges. This can be seen visually by calculating and comparing the residuals of the image beyond 20 kpc for each model. Significant deviations are only seen in the lower two mass bins. The fits to the lowest mass bin is not perfect due to limited number of galaxy images (~ 1212) which went into the stack. At first glance, our conclusion that a double-Sérsic profile is *always* required may seem surprising, because the surface brightness profiles of massive galaxies with high concentration do not exhibit a clear inflexion point. We note that a single-Sérsic model has a single fixed ellipticity, while the double-Sérsic model with different ellipticities for each component can in a limited way mimic the varying ellipticity of the stacked galaxy image. We investigated whether the change in ellipticity is the dominant factor that favours a double-Sérsic profile over a single-Sérsic profile. To test this, we compare a single-Sérsic and a double-Sérsic profile fitted to similar stacks of galaxies which are not aligned but are randomly oriented. In all cases, the double

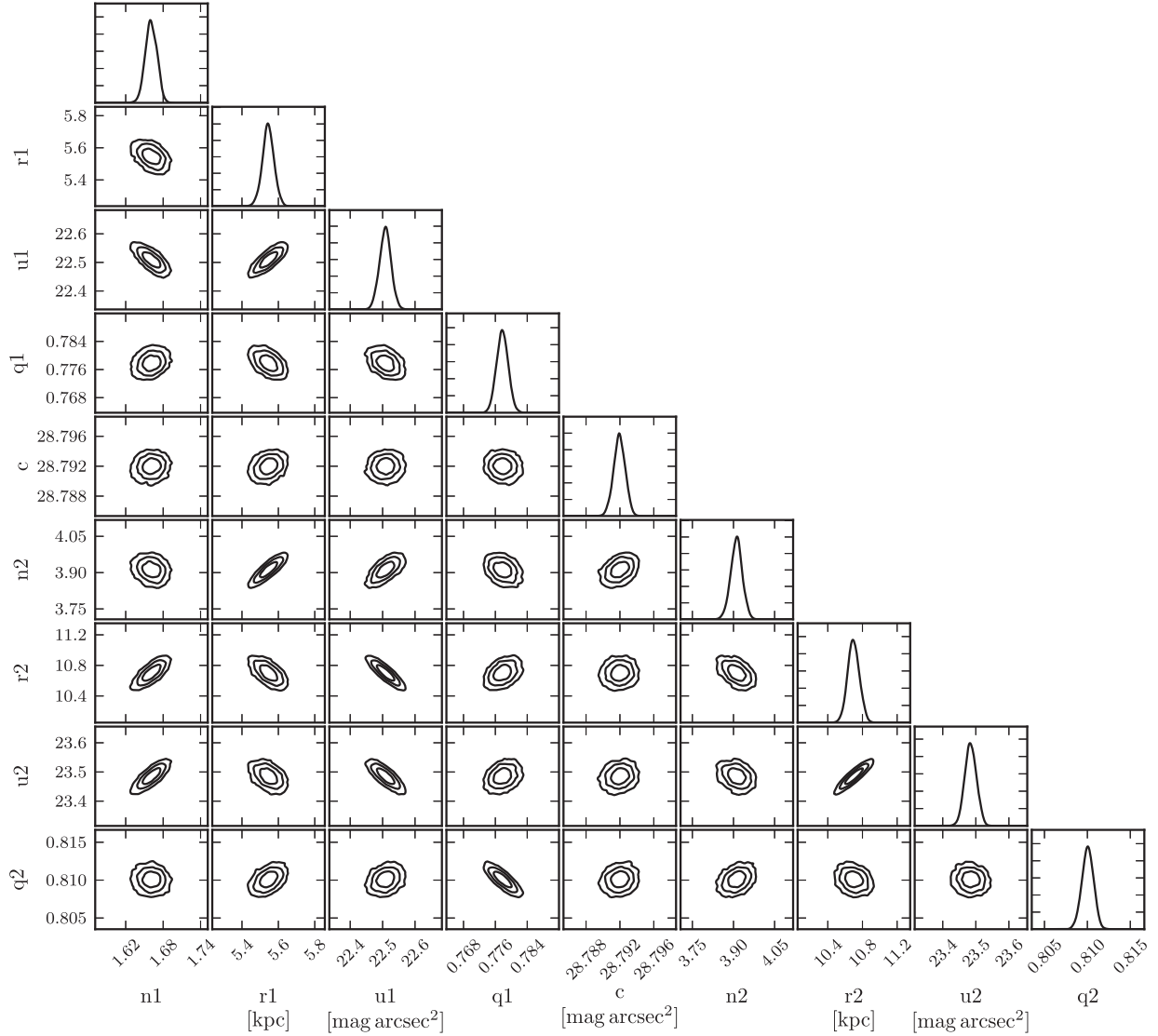


Figure 12. The probability distribution function (PDF) and the correlations between the various parameters of the double-Sérsic model (see Table 1) for the high-concentration highest stellar mass bin stack ($C > 2.6, 10^{11.0} M_{\odot} < M_{*} < 10^{11.4} M_{\odot}$). The effective intensity and the residual sky value are expressed in units of mag arcsec^{-2} .

Sérsic is still preferred over the single-Sérsic profile. The factor $2\log_e(B_{D/S})$ in the randomly oriented case is reduced to one-third of that as calculated in Table 2. This indicates that it is both the surface brightness profile and the ellipticity which contribute to favour a double-Sérsic profile over a single-Sérsic profile.

Plots of the Sérsic indices of the two components as a function of mass are shown in Fig. 13. The outer Sérsic index increases with the mass of the galaxy stack from $n \sim 3$ to ~ 4 . The effective radii of each component are also denoted in the Fig. 13. The effective radius of the outer component scales as $\propto 2.5 \log_{10} M_{*}$ reaching a maximum of 9 kpc for the highest mass bins. We note that the inner Sérsic component is always more elliptical than the outer Sérsic component. On the other hand, the inner ellipticity profiles derived in Fig. 4 are significantly affected by the PSF. The ellipticity of the inner component is approximately constant for all mass bins while the ellipticity of the outer component increases as mass increases.

Having separated the light from the galaxy into two components, we study the variation of the light in the two components as a function of stellar mass. We can also calculate the fraction of light

in the outer Sérsic component (Fig. 14). We will discuss this result in Section 7.

5.2 Low-concentration galaxy stacks

Modelling low-concentration galaxies along with their stellar halo component remains a challenging task, because of the extremely low fraction of light in the stellar halo in these systems. Estimates of the stellar halo contribution for M31 lie between 0.6 and 1.5 per cent (Ibata et al. 2014), while those for the Milky Way lie between 0.3 and 1.0 per cent (Bell et al. 2003; McMillan 2011). Previous modelling and estimates of the stellar halo content of disc galaxies have been made from star counts. In order to detect the stellar halo in face-on disc galaxies, deep imaging is necessary with an accurate determination of the background residuals. Recently, van Dokkum et al. (2014) tried to model and determine the stellar halo content of the massive spiral galaxy M101 from integrated surface brightness profiles by going to a depth of $\mu_g \sim 32 \text{ mag arcsec}^{-2}$. The effective depths of our stacked images are similar to this.

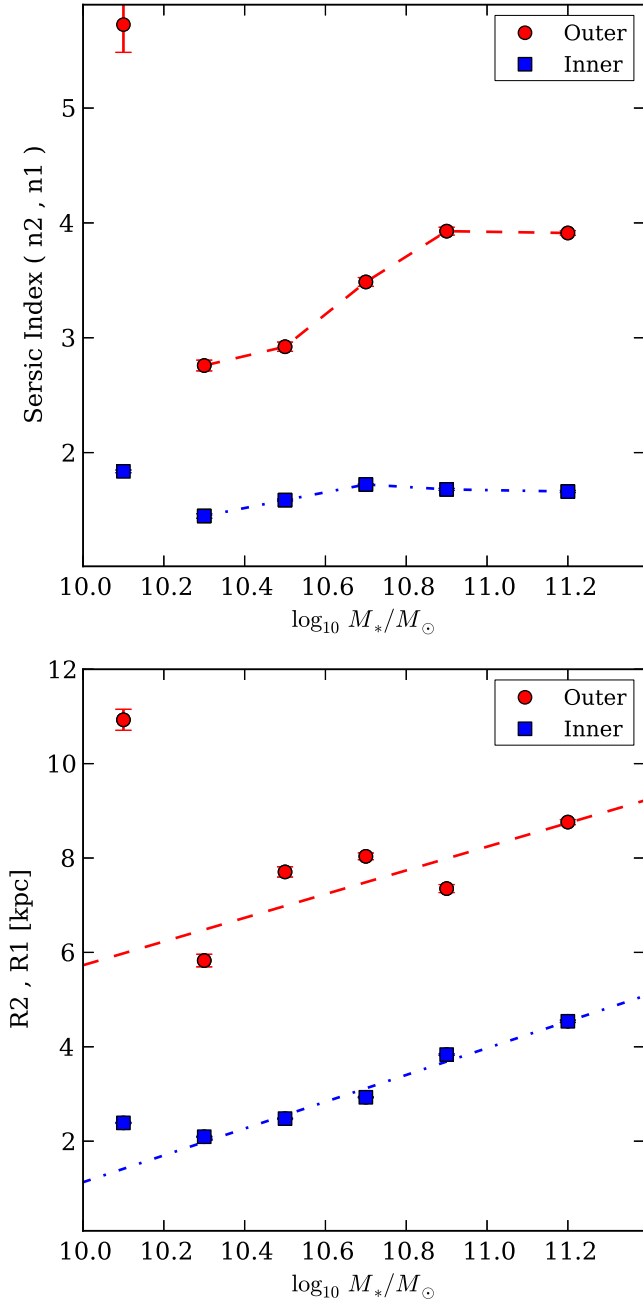


Figure 13. (a) The Sérsic indices of the inner(blue) and outer(red) components for high-concentration galaxies. (b) The effective radii of the inner (blue) and outer (red) Sérsic components for high-concentration galaxies. The outer effective radius scales as $\propto 2.5 \log_{10} M_*$ while the inner effective radius scales as $\propto 2.8 \log_{10} M_*$. The model fails to fit for the lowest mass bin because of insufficient numbers in the stack.

Another important issue is that disc breaks in galaxies (Bakos et al. 2008) also cause inflections in the surface brightness profile of the stacked galaxies and need to be modelled. We find that a double-Sérsic model often fails to fit the stacks of low-concentration galaxies, as is shown in Fig. 15. In these galaxies, the inflection is caused by disc breaks and these breaks can occur very close to where the stellar halo becomes dominant.

A natural extension of our modelling procedure would be to use a concentric triple-Sérsic model. However, the general triple-Sérsic model is highly degenerate, especially when trying to separate com-

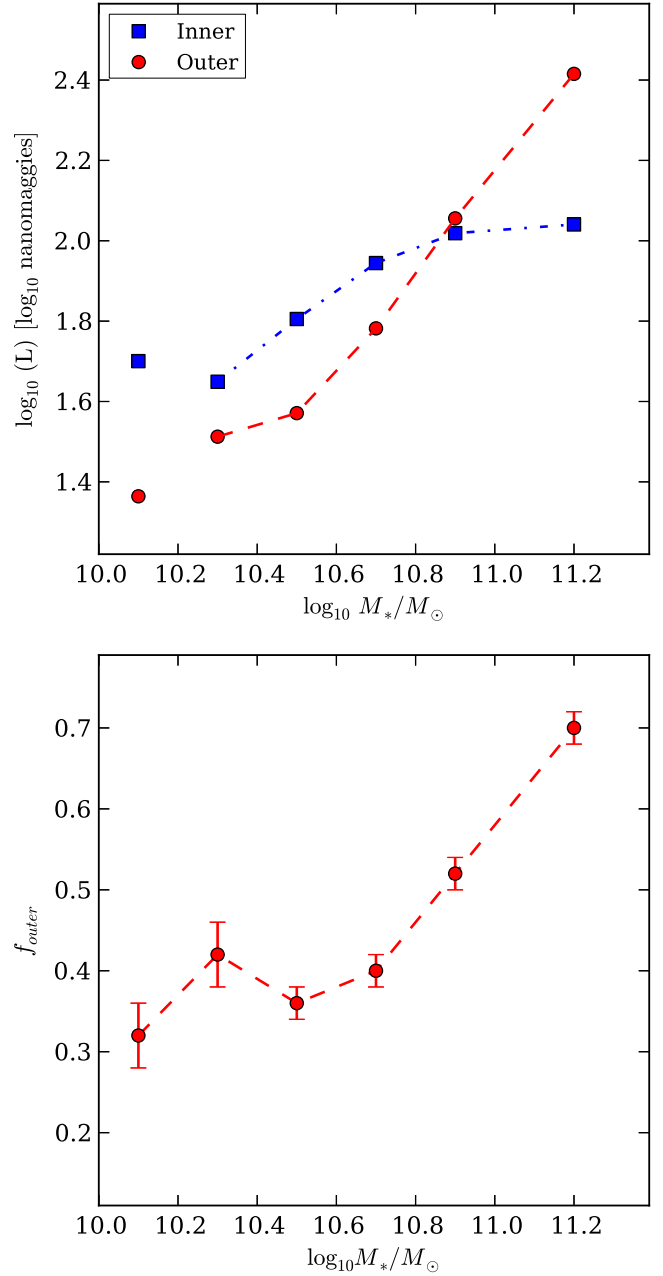


Figure 14. (a) The \log_{10} of the r -band total luminosity (in nanomaggies) in the inner (blue) and outer (red) components as a function of stellar mass for high-concentration galaxies. (b) The fraction of light in the outer Sérsic component as function of stellar mass for high-concentration galaxies.

ponents which are not easily distinguishable from each other. Face-on disc galaxies with a low stellar-halo mass fraction occupy only a limited parameter space of a three-component model. To break these degeneracies, we truncate the inner two components (beyond $7-8R_e$) and apply restrictions to the third component of the triple-Sérsic model. In particular, we look for third component solutions that involve a low Sérsic index ($n_3 < 1.5$), lower effective intensity (in comparison to the other two components) and a larger effective radius ($R_e > 15$ kpc) for the outermost component. The low Sérsic index ensures that the profile of the third outer component does not rise steeply and dominate the inner central parts of the galaxy. The parameters of the triple-Sérsic model are summarized in Table 3.

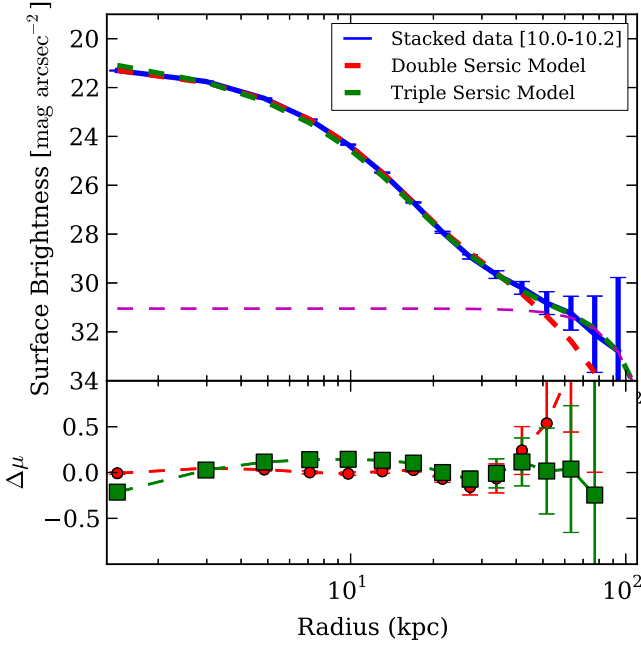


Figure 15. The double-Sérsic model (shown in red) provides an inadequate fit to low-concentration ($C < 2.6$) low-mass galaxies ($10^{10.0} M_{\odot} < M_* < 10^{10.2} M_{\odot}$). The triple-Sérsic model provides a much better fit (shown in green). The third component of the triple-Sérsic model is shown in a dashed magenta line. In the bottom panel, the residuals of the double-Sérsic model and the triple-Sérsic model are shown.

Table 3. Parameters of the triple-Sérsic model.

Triple Sérsic	
$n1$	Inner Sérsic index
$r1$	Inner effective radius
$i1$	Inner effective intensity
$q1$	Inner ellipticity
c	Residual sky value
$n2$	Middle Sérsic index
$r2$	Middle effective radius
$i2$	Middle effective intensity
$q2$	Middle ellipticity
$n3$	Outer Sérsic index
$r3$	Outer effective radius
$i3$	Outer effective intensity
$q3$	Outer ellipticity

We also modify our fitting algorithm as follows. We do not fit three components at the same time. We first model independently the galactic disc along with the disc break in high S/N part of the stacked image with a truncated double-Sérsic model. Later, having fixed the two components describing the internal part of the galaxy, we add a third component to model the outer extra light. This is necessary because the S/N of the light of the outer image is so much lower than that of the inner regions. If the disc break occurs close to the where the stellar halo becomes dominant (i.e. if the stellar halo fraction is not negligible), we first model the internal two components with a truncated double-Sérsic model. Then keeping the innermost component fixed, we model the disc break and the extra stellar halo light by fitting two additional Sérsic components. In both methods, we determine the constant sky component at each step. The restriction of a low Sérsic index for the outer component

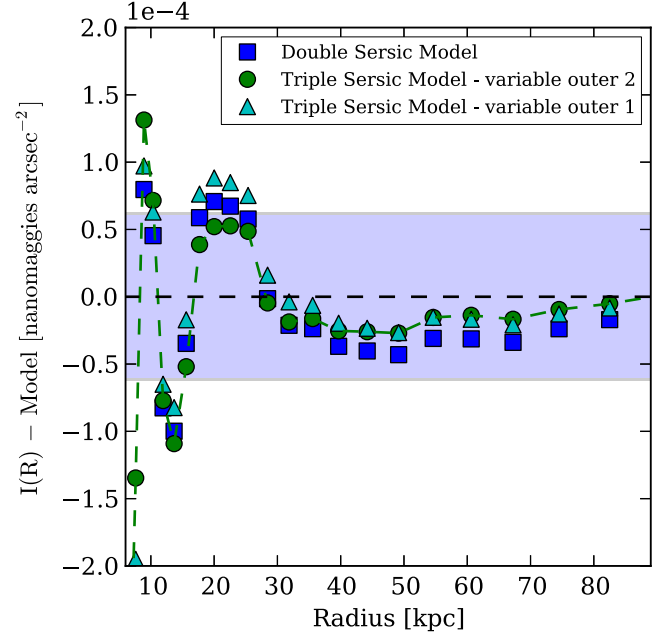


Figure 16. The residuals for three models: the double Sérsic, the triple Sérsic by keeping the innermost component fixed (Method A) and the triple Sérsic by keeping the inner two components fixed (Method B) for galaxies stacked in the mass bin range $10^{10.0} M_{\odot} < M_* < 10^{10.2} M_{\odot}$ and with concentration $C < 2.6$. The fraction of light of the galaxy in the outermost component by Method A is 2.3 ± 0.4 per cent and by method B is 1.2 ± 0.3 per cent. The blue band gives the average uncertainty in the background removal for each pixel in nanomaggies arcsec $^{-2}$.

does not significantly affect our results as the fixing of the inner component automatically reduces the value of the outer Sérsic index.

The global Bayes factor is unable to differentiate between models in the low-concentration case, since it is dominated by the asymmetric component (bars, pseudo-bulges, etc.) at the centre of the stacked galaxy. In order to judge which fitting method is most appropriate for a given galaxy stack, we subject every image stack to both methods and calculate the chi-square of the image for each pixel beyond 20 kpc. We compare the reduced chi-square for a double-Sérsic model, as well as both methods for determining the third component of the triple-Sérsic model, and choose the best-fitting model. In Fig. 16, we compare the residuals of the double-Sérsic model as well as the two methods for determining the components of the triple-Sérsic model for disc galaxies stacked in the mass bin range $10^{10.2} M_{\odot} < M_* < 10^{10.4} M_{\odot}$, with concentration index $C < 2.6$. The blue band gives the average uncertainty in background removal for each pixel in nanomaggies arcsec $^{-2}$. The procedure which keeps the innermost component fixed and varies the outer two components fares the best. The best-fitting triple-Sérsic model is shown in Fig. 15.

The accuracy of modelling the third component depends upon the accuracy of the correct background sky determination. This accuracy is limited by the accuracy of our background removal. For the model fits to the stack of $N \sim 3000$ galaxy images shown in Fig. 15, if we assume a conservative Sérsic index ($n \sim 0.4$) and an effective radius $R_e \sim 40$ kpc and an effective magnitude determined by the error of the background residuals ($I_e \sim 6 \times 10^{-5}$ nanomaggies arcsec $^{-2}$), the third component can be correctly determined if it is greater than 2 per cent of the total light in the galaxy.

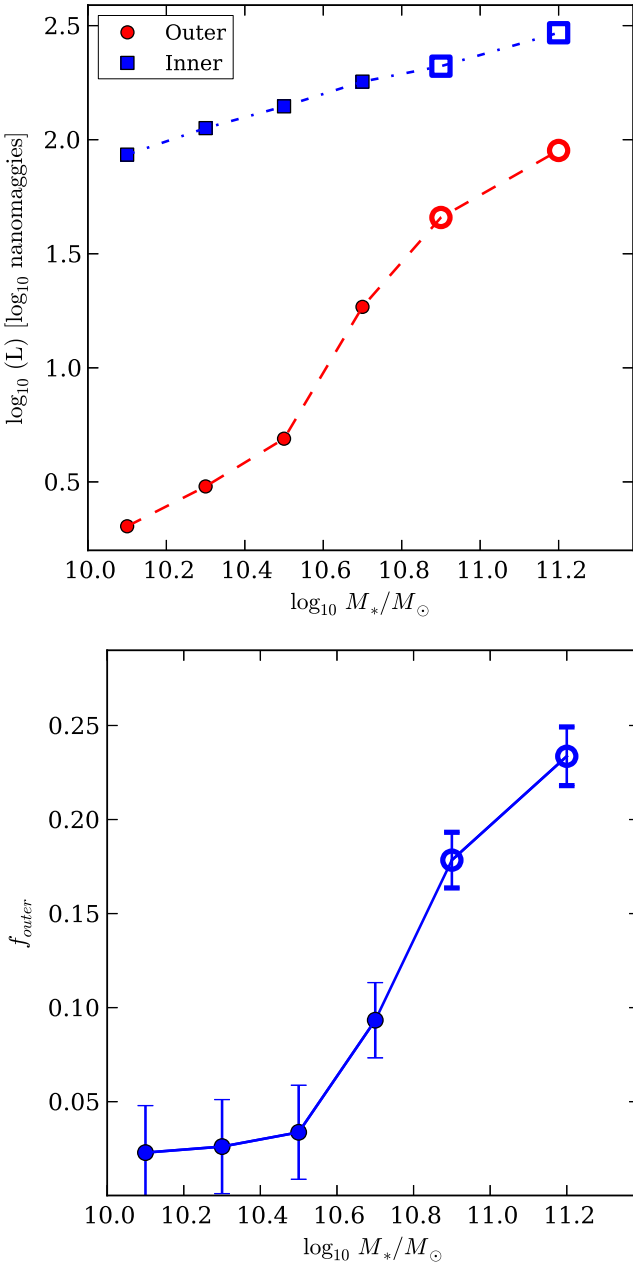


Figure 17. (a) The \log_{10} of the r -band total luminosity (in nanomaggies) in the inner (blue) and outermost (red) components as a function of stellar mass for low-concentration galaxies. (b) The fraction of light in the outermost Sérsic component as a function of stellar mass for low-concentration galaxies. The hollow circular markers indicate that a triple-Sérsic profile was required to model the outer parts of the stellar halo, while the filled circular markers indicate that a double-Sérsic profile was sufficient.

In Fig. 17, we plot the fraction of the total light and stellar mass of the galaxy in the inner and outermost components. Results are shown as a function of M_* and for low- and high-concentration systems. For low-concentration galaxies, the higher two mass bins are best fit by double-Sérsic models, while the lower mass bins are best fit by triple-Sérsic models. Most of the low-concentration stacks which are modelled successfully by a triple-Sérsic profile are best fit by keeping only the innermost component fixed. Only one low-concentration stack ($10^{10.0} M_\odot < M_* < 10^{10.2} M_\odot$) could be

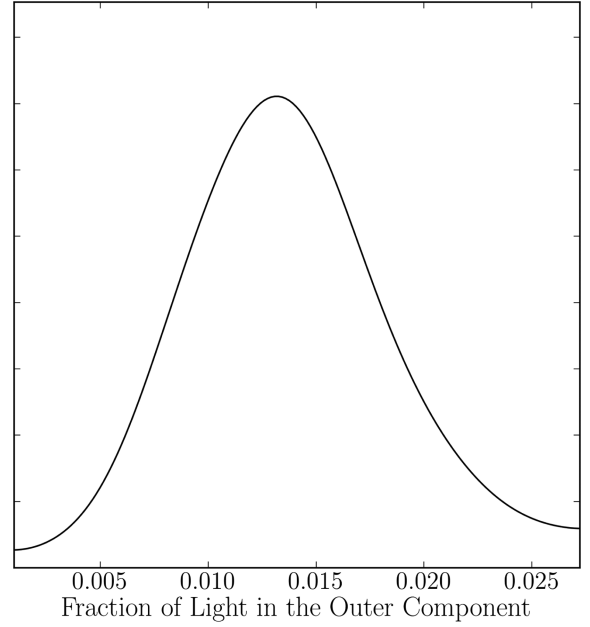


Figure 18. The probability distribution function (PDF) of f_{outer} for the stacked image of disc galaxies in the mass range $10^{10.0} M_\odot < M_* < 10^{10.8} M_\odot$ and with a concentration of $C < 2.6$.

best fit by fixing the inner two Sérsic components. We will discuss these results later in Section 7.

Improved accuracy in determining the third component may be obtained by stacking a larger number of low-concentration galaxies. We stack 12 423 galaxies in the r band with random orientations in the mass range $10^{10.0} M_\odot < M_* < 10^{10.8} M_\odot$, with a concentration $C < 2.4$ and with an isophotal axial ratio ≥ 0.77 . Using our modelling procedure, we can derive the PDF of the fraction of light in the third component (see Fig. 18). This fraction is about 1.3 ± 0.5 per cent.

Our modelling allows us to identify a radius at which the outer component begins to dominate the integrated stellar light (R_{acc}). In Fig. 19, the blue squares indicate this radius as a function of M_* for low-concentration galaxies. As can be seen, this radius *decreases* as a function of the stellar mass of the galaxy from ~ 50 kpc for galaxies with stellar masses of a few times $10^{10} M_\odot$ to ~ 30 kpc for galaxies with $M_* \sim 10^{11} M_\odot$. For comparison, we also compare R_{acc} with the radius at which the minimum occurs in the $g - r$ colour profiles of low-concentration galaxies ($R_{\text{colour min}}$; see Fig. 7). The radius at which the outer material begins to dominate is much larger than the radius at which the minimum in the colour profile occurs. This accords well with suggestions in the literature that this minimum in the $g - r$ colour profile is associated with the break radius in disc galaxies (Bakos et al. 2008).

Also in Fig. 19, we compare the radius at which the outer material begins to dominate with the radius at which the $g - r$ colour profile flattens for high-concentration galaxies. The radius at which the $g - r$ colour profile flattens increases as a function of stellar mass from ~ 20 kpc for galaxies with stellar masses of a few times $10^{10} M_\odot$ to ~ 40 kpc for galaxies with $M_* \sim 10^{11} M_\odot$. The radius at which the outer material begins to dominate is comparatively smaller and decreases as a function of stellar mass. For the highest stellar bin, this radius approaches close to the centre of the galaxy indicating that the outer accreted material is spread all over the galaxy.

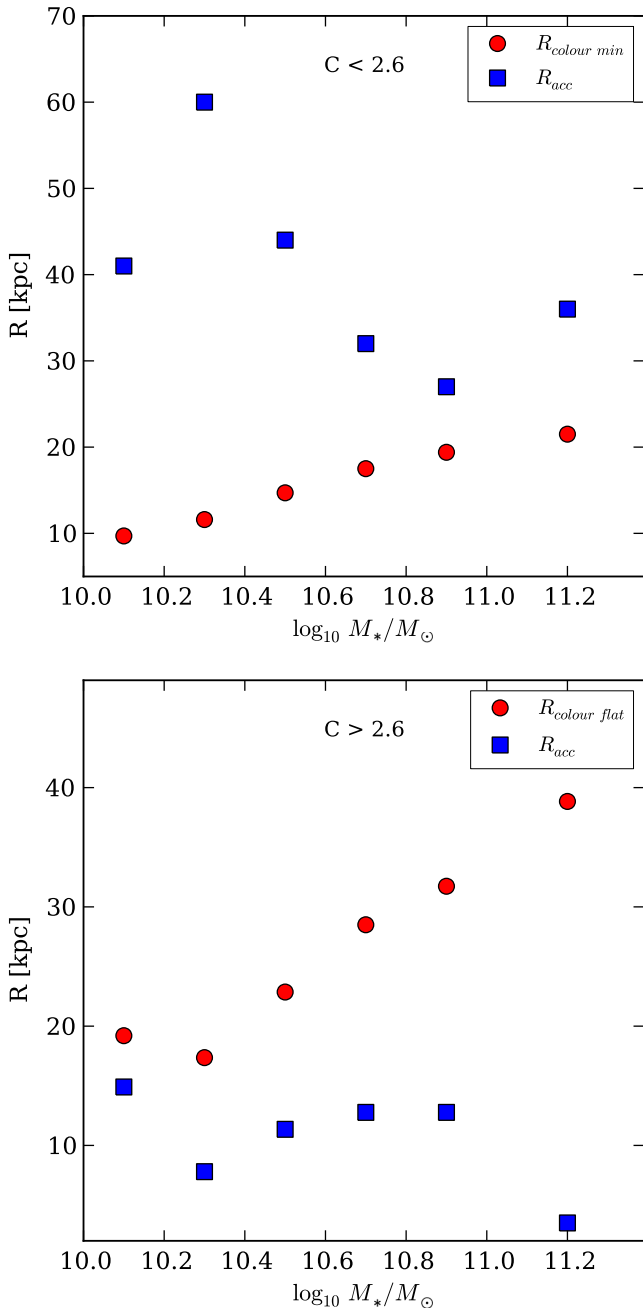


Figure 19. (a) and (b) The radius at which the accreted component begins to dominate over the *in situ* component (R_{acc}) for low-concentration and high-concentration galaxies as a function of stellar mass (blue squares). Also shown is the radius at which there is a minimum in the $g-r$ colour profiles ($R_{colour\ min}$) for low-concentration galaxies and the radius at which the $g-r$ colour profile ($R_{colour\ flat}$) flattens for high concentration as a function of stellar mass (red circles).

6 SUMMARY

In this work, we have shown that stacking g - and r -band mosaics of similar galaxies allows us to derive reliable surface brightness profiles up to a depth of $\mu_r \sim 32 \text{ mag arcsec}^{-2}$. We study surface brightness, ellipticity and $g-r$ colour profiles as a function of stellar mass and galaxy type. We perform fits to the stacked images using multicomponent Sérsic models. This enables us to estimate the fraction of the stellar light/mass in the outermost component,

which we hypothesize to be built up from accreted stellar material, and to set constraints on theories for the formation of stellar haloes through hierarchical merging.

The main results of this paper can be summarized as follows.

- (i) The fraction of accreted stellar material increases with stellar mass. At fixed mass, the fraction of accreted material is higher in early-type than in late-type galaxies.
- (ii) The stellar haloes of high-concentration galaxies ($C > 2.6$) tend to be more elliptical than those of low-concentration galaxies ($C < 2.6$). The ellipticity of the outer stellar halo increases strongly with stellar mass for high-concentration galaxies, and more weakly with stellar mass for low-concentration galaxies.
- (iii) Because we stack galaxies that are nearly face-on, we are only able to probe the colour of the outer accreted component in high-concentration galaxies. In these systems, the $g-r$ colour of the outer halo light is bluer than the centre of the galaxy and is an increasing function of stellar mass.
- (iv) We find that a single-Sérsic profile cannot fit the entire two-dimensional surface brightness distribution of any of our stacked images. Multicomponent models are needed to model the excess light in the outer parts of the galaxy, especially between $\mu_r \sim 28$ and $32 \text{ mag arcsec}^{-2}$, and to account for the radial dependence of the ellipticity of the light distribution.
- (v) Double-Sérsic profiles adequately model the surface brightness distributions of high-concentration galaxies ($C > 2.6$), while triple-Sérsic profiles are often needed to model the surface brightness profile of low-concentration galaxies ($C < 2.6$).
- (vi) Using the fraction of light in the outer component of our models as a measure of the fraction of the total stellar mass composed of accreted stellar material, we find that this fraction is an increasing function of stellar mass. At fixed stellar mass, it is also a function of concentration. For high-concentration galaxies, the fraction of accreted stellar light rises from 30 to 70 per cent, while for low-concentration galaxies the fraction of stellar light rises from 2 to 25 per cent for galaxies in the stellar mass range $10^{10.0} M_\odot$ – $10^{11.4} M_\odot$.

7 DISCUSSION

We have attempted to characterize the stellar halo of galaxies through modelling their surface brightness. It is the depth, the large dynamic range and the two-dimensional shape information (ellipticity) of our surface brightness profiles which enables us to recognize deviations from a single-component profile and to model successfully the stellar halo of our galaxy stacks out to 100 kpc with two or three components.

An important outcome is that a single-Sérsic component cannot fit the surface brightness profiles of high-concentration galaxies over a large dynamic range in radius and surface brightness, but can only fit the inner parts of galaxies. The inability of a single Sérsic to fit the two-dimensional surface brightness profile of galaxies has also been confirmed by the studies of Bernardi et al. (2013), Simard et al. (2011) and Lackner & Gunn (2012). Multicomponent models are needed to model the full two-dimensional surface brightness profiles of galaxies. We have demonstrated that it is both the average shape of the surface brightness profile and the radial variation in ellipticity of the light in a galaxy stacks that constrain such models.

For high-concentration galaxies, the effective radius of the outer component is twice as large as the effective radius of the inner component. For low-concentration galaxies, the effective radius of

the outer component is much larger than the inner components. For high-concentration galaxies, the luminosity of the outer component is a significant fraction of the total luminosity of the galaxy and ranges from 30 to 70 per cent. It also dominates over a large radial range of the galaxy. On the other hand, in low-concentration galaxies, the outer component occupies a smaller fraction (from 2 to 25 per cent) and is only dominant at radii larger than 20–30 kpc. In both cases, the fraction of light in the outer component increases with stellar mass (see the red line in the top plots of Figs 17 and 14).

We propose in this work that the fraction of light in the outer component provides a measure of the amount of accreted stellar light in the galaxy. While a direct one-to-one correspondence between the fraction of light in the outer component and the fraction of accreted stellar light cannot be directly proven, the trends in the fraction of light in the outer component agree qualitatively with the trends of the accreted light fraction as a function of mass and galaxy-type in the particle-tagging models of Cooper et al. (2013). Interestingly, the rate of increase of accreted stellar mass increases dramatically above $M_* \sim 10^{10.6} M_\odot$. This corresponds to the stellar mass where galaxies transition from blue/star-forming to red/passive systems (Kauffmann et al. 2003b). A significant jump in the accreted mass fraction may be most simply explained by *in situ* growth of the galaxy being terminated by feedback processes, such as energy injection from relativistic jets produced by black holes in massive galaxies (Croton et al. 2006). In the two-stage model of massive galaxy formation proposed by Oser et al. (2010), an early, rapid *in situ* star formation period is followed by a late merger-dominated period. In the later phase, galaxies tend to grow predominately through minor mergers. We note that the particle-tagging models of Cooper et al. (2013) are directly tied to semi-analytic models that include AGN feedback prescription, and thus also include quenching of *in situ* growth of galaxies through cooling and star formation. In future work, we intend to undertake a detailed comparison with these models.

Measuring the ellipticity of the outer stellar halo of galaxy also provides us with hints about the formation processes for the stellar halo. A high ellipticity is likely to imply that satellite systems are preferentially accreted along the major axis of the main galaxy (Tal & van Dokkum 2011). The variance in the outer stellar halo profile between different galaxies can be predicted from our surface brightness profiles. This variance results from the fact that similar galaxies can have stellar haloes with very different masses, sizes and shapes. The physical origin of this variance as predicted by the Λ CDM models, is that galaxies of the same mass have had a range of merger histories, resulting in different accreted stellar mass fractions. This has also been clearly demonstrated using particle-tagging techniques on the Aquarius haloes (Cooper et al. 2010), which show very large halo-to-halo differences.

We also note that the integrated surface brightness of the galaxy, including the stellar halo, includes considerably more light than measured by the SDSS model and cModel magnitudes. For example, for high-concentration galaxies in the stellar mass range $10^{11.0} M_\odot < M_* < 10^{11.4} M_\odot$, there is about 50 per cent more light contained in the stellar halo at surface brightnesses greater than $\mu_r \sim 24.5 \text{ mag arcsec}^{-2}$. This implies that there is considerably more stellar material in the galaxy than one might infer from the SDSS photometry. The stellar masses defined by the MPA-JHU catalogue and used in this work are only used to define the stellar mass bins, and are systematically less than the true stellar mass of the galaxy. This will also be the subject of future work.

ACKNOWLEDGEMENTS

Funding for SDSS-III has been provided by the Alfred P. Sloan Foundation, the Participating Institutions, the National Science Foundation, and the US Department of Energy Office of Science. The SDSS-III website is <http://www.sdss3.org/>.

SDSS-III is managed by the Astrophysical Research Consortium for the Participating Institutions of the SDSS-III Collaboration including the University of Arizona, the Brazilian Participation Group, Brookhaven National Laboratory, University of Cambridge, Carnegie Mellon University, University of Florida, the French Participation Group, the German Participation Group, Harvard University, the Instituto de Astrofísica de Canarias, the Michigan State/Notre Dame/JINA Participation Group, Johns Hopkins University, Lawrence Berkeley National Laboratory, Max Planck Institute for Astrophysics, Max Planck Institute for Extraterrestrial Physics, New Mexico State University, New York University, Ohio State University, Pennsylvania State University, University of Portsmouth, Princeton University, the Spanish Participation Group, University of Tokyo, University of Utah, Vanderbilt University, University of Virginia, University of Washington and Yale University.

REFERENCES

- Bakos J., Trujillo I., Pohlen M., 2008, *ApJ*, 638, 103
- Bell E. F., McIntosh D. H., Katz N., Weinberg M. D., 2003, *ApJS*, 149, 289
- Bell E. F. et al., 2008, *ApJ*, 680, 295
- Bender R., Burstein D., Faber S. M., 1992, *MNRAS*, 399, 462
- Bergvall N., Zackrisson E., Caldwell B., 2010, *MNRAS*, 405, 2697
- Bernardi M., Meert A., Sheth R. K., Vikram V., Huertas-Company M., Mei S., Shankar F., 2013, *MNRAS*, 436, 697
- Bertin E., Arnouts S., 1996, *A&AS*, 117, 393
- Bertin E., Mellier Y., Radovich M., Missonnier G., Didelon P., Morin B., 2002, in Bohlender D. A., Durand D., Handley T. H., eds, *ASP Conf. Ser. Vol. 281, Astronomical Data Analysis Software and Systems XI*. Astron. Soc. Pac., San Francisco, p. 228
- Blanton M. R. et al., 2003, *ApJ*, 592, 819
- Blanton M. R., Kazin E., Muna D., Weaver B. A., Price-Whelan A., 2011, *AJ*, 142, 31
- Bullock J. S., Johnston K. V., 2005, *ApJ*, 635, 931
- Cooper A. P. et al., 2010, *MNRAS*, 406, 74
- Cooper A. P., D'Souza R., Kauffmann G., Wang J., Boylan-Kolchin M., Guo Q., Frenk C. S., White S. D. M., 2013, *MNRAS*, 434, 3348
- Croton D. J. et al., 2006, *MNRAS*, 365, 11
- de Jong R. S., 2008, *MNRAS*, 388, 1521
- de Vaucouleurs G., 1948, *Ann Astrophys.*, 11, 247
- Feroz F., Hobson M. P., Bridges M., 2008, *MNRAS*, 398, 1601
- Feroz F., Hobson M. P., Cameron E., Pettitt A. N., 2013, preprint ([arXiv:1306.2144](https://arxiv.org/abs/1306.2144))
- Fremman K. C., 1970, *AJ*, 160, 811
- Gonzalez-Perez V., Castander F. J., Kauffmann G., 2011, *MNRAS*, 411, 1151
- Huang S., Ho L. C., Peng C. Y., Li Z.-Y., Barth A. J., 2013, *ApJ*, 766, 47
- Hubble E. P., 1936, *Realm of the Nebulae*. Yale Univ. Press, New Haven, CT
- Ibata R. A. et al., 2014, *ApJ*, 780, 128
- Kass R. E., Raftery A. E., 1995, *J. Am. Stat. Assoc.*, 90, 773
- Kauffmann G. et al., 2003a, *MNRAS*, 341, 33
- Kauffmann G. et al., 2003b, *MNRAS*, 341, 54
- Kelly B. C., 2007, *ApJ*, 665, 1489
- Kormendy J., 1977, *ApJ*, 217, 406
- Kormendy J., Fisher D. B., Cornell M. E., Bender R., 2009, *ApJS*, 182, 216
- La Barbera F., Ferreras I., de Carvalho R., Bruzual G., Charlot S., Pasquali A., Merlin E., 2012, *MNRAS*, 426, 2300
- Lackner C. N., Gunn J. E., 2012, *MNRAS*, 421, 2277

- Lackner C. N., Cen R., Ostriker J. P., Joung M. R., 2012, *MNRAS*, 425, 641
 McMillan P. J., 2011, *MNRAS*, 414, 2446
 Malin D. F., Carter D., 1983, *ApJ*, 274, 534
 Martinez-Delgado D. et al., 2010, *AJ*, 140, 962
 Mihos J. C., Harding P., Feldmeier J., Morrison H., 2005, *ApJ*, 631, L41
 Monachesi A. et al., 2013, *MNRAS*, 426, 106
 Mosleh M., Williams R., Franx M., 2013, *ApJ*, 777, 117
 Oser L., Ostriker J. P., Naab T., Johansson P. H., Burkert A., 2010, *ApJ*, 725, 2312
 Peng C. Y., Ho L. C., Impey C. D., Rix H.-W., 2010, *AJ*, 139, 2097
 Pohlen M., Trujillo I., 2006, *A&A*, 454, 749
 Purcell C. W., Bullock J. S., Zentner A. R., 2007, *ApJ*, 666, 20
 Schlegel D. J., Finkbeiner D. P., Davis M., 1998, *ApJ*, 500, 525
 Schweizer F., 1980, *ApJ*, 237, 303
 Schweizer F., Seitzer P., 1992, *AJ*, 104, 1039
 Sérsic J. L., 1968, *Atlas de Galaxies Australes*. Observatorio Astronomico, Univ. Cordoba, Cordoba
 Sesar B., Jurić M., Ivezić Ž., 2011, *ApJ*, 731, 4
 Simard L., Mendel J. T., Patton D. R., Ellison S. L., McConnachie A. W., 2011, *ApJS*, 196, 11
 Strateva I., Ivezić Ž., Knapp G. R., 2001, *AJ*, 122, 1861
 Suh H., Jeong H., Oh K., Yi S. K., Ferreras I., Schawinski K., 2010, *ApJS*, 187, 374
 Tal T., van Dokkum P. G., 2011, *ApJ*, 731, 89
 Tal T., van Dokkum P. G., Nelan J., Bezanson R., 2009, *AJ*, 138, 1417
 Tortora C., Napolitano N. R., Cardone V. F., Capaccioli M., Jetzer Ph., Molinaro R., 2010, *MNRAS*, 407, 144
 van Dokkum P. G., Abraham R., Merritt A., 2014, *ApJ*, 782, 24
 Wang W., White S. D. M., 2012, *MNRAS*, 424, 2574
 Yoon I., Weinberg M. D., Katz N., 2011, *MNRAS*, 414, 1625
 Zibetti S., White S. D. M., Brinkmann J., 2004, *MNRAS*, 347, 556
 Zibetti S., White S. D. M., Schneider D. P., Brinkmann J., 2005, *MNRAS*, 358, 949

APPENDIX A: THE AMOUNT OF LIGHT MISSED

The masking procedure we have employed is far from perfect. Contamination may arise from the incomplete masking of unresolved sources. An estimate of the amount of light missed as a function of environment can be made by creating mock galaxy images from an appropriate Schechter luminosity function for that environment. For the purpose of estimating how much of unresolved sources is not masked out in our field environment, we generate 1000 realistic mock galaxy *r*-band images resembling the field environment of our Sample by using a fixed single-Sérsic model for the main central galaxy and the parameters of the *r*-band Schechter luminosity function of Blanton et al. (2003) for the galaxy environment. Each galaxy image was convolved with the SDSS *r*-band PSF. In addition, Poisson noise was added to each image.

After subjecting these mocked images to our masking/stacking procedure outlined in the paper, we try to recover the surface brightness profile of the central galaxy. We find that we recover surprisingly well the surface brightness profile over a large range of the galaxy as seen in Appendix A1. PSF effects come into play at the centre of the galaxy, while the profile in the faint outer parts depends on the accuracy of the background subtraction.

Our recovery of surface brightness profile can be attributed to a number of factors: First of all, the relatively low-density environment of field galaxies help in the masking procedure. Secondly, multiple runs of SExtractor help us to mask out most of the overlapping galaxies. Thirdly, the percentile cuts we have used in the stacking procedure helps us to deal with failures in the masking procedure especially close to the main galaxy.

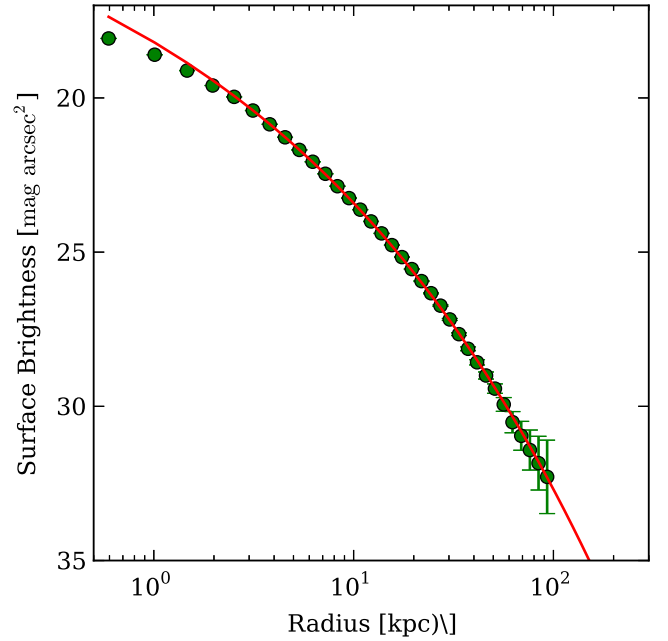


Figure A1. Recovered luminosity profiles from the mock images. The red line is the initial model convolved with the *r*-band PSF.

APPENDIX B: MEASUREMENT OF THE OUTER SLOPE

To measure the outer slope (m) of the surface brightness profile, we consider a hierarchical Bayesian methodology that takes into consideration measurement errors and the intrinsic scatter in the slope σ (Kelly 2007). Following equation (2), we can write the likelihood for each measurement y_i with measurement error δy_i as

$$p(y_i | \theta) = \frac{1}{\sqrt{2\pi(\delta y_i^2 + \sigma^2)}} \exp \left\{ -\frac{1}{2} \frac{[y_i - E(y_i | \theta)]^2}{\delta y_i^2 + \sigma^2} \right\}, \quad (\text{B1})$$

where $E(y_i | \theta) = 10^{m \log x_i + c}$.

Following Kelly (2007), we use uniform priors in m (−10: 10), c (−100: 100) and σ^2 (10^{-8} : 1). We calculate the posterior PDF of each parameter using MULTINEST. For the final parameters, we report the maximum of the posterior PDF. The uncertainty in the reported parameter is calculated from the variance of the posterior PDF.

APPENDIX C: THE INFLUENCE OF THE PSF ON THE COLOUR PROFILES

The $g - r$ colour profiles in Figs 6 and 7 have been derived without convolving for the PSF. We have justified this on the basis of the small difference between the PSF in the g and r band as shown in Fig. 3. In order to investigate the effect of the PSF on the colour profiles, we also derive the colour profile through a parametric method from the model fits as done by La Barbera et al. (2012) for early-type galaxies. We first fit models to both the g and r bands (as demonstrated in Section 5). In Fig. C1, we derive the $g - r$ colour profiles directly from the models fits to the g and r band image stacks. These parametric colour profiles are devoid of the effects of the PSF. They display the same trends as the non-parametric colour profiles as derived in Section 4.3. There are small differences (within the error bars) in the colour profiles close to the centre of the galaxy stack. These differences increase for higher stellar mass bin stacks.

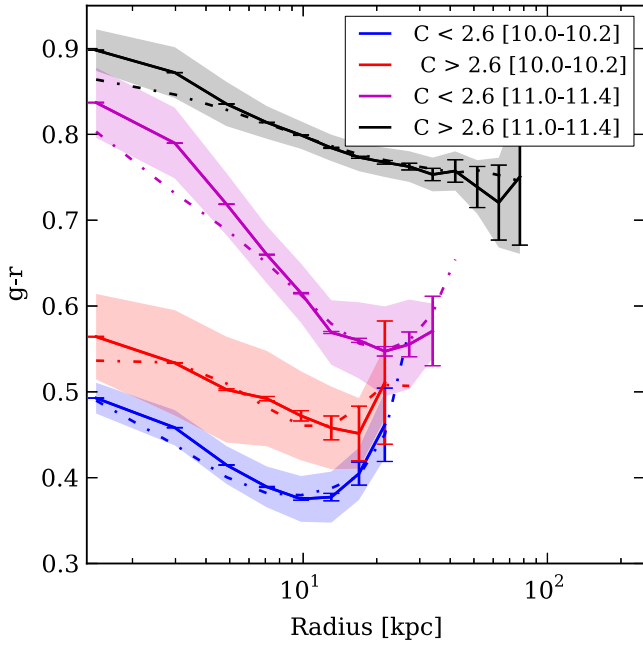


Figure C1. The $g-r$ colour profiles derived directly (solid lines) and through the parametric method (dot-dashed lines) for high and low-concentration galaxies in the stellar mass bin range $10^{10.0} M_{\odot} < M_{*} < 10^{10.2} M_{\odot}$ and $10^{11.0} M_{\odot} < M_{*} < 10^{11.4} M_{\odot}$.

This is due to the fact that the models in Section 5 provide a poor fit at the centre of the galaxy stacks because of the high variance and the asymmetries present. This demonstrates that the $g-r$ colour profiles derived in Section 4.3 are robust. This is also consistent with the conclusions of La Barbera et al. (2012) that the PSF does not affect the $g-r$ colour profile a lot (fig. 3 of La Barbera et al. 2012).

This paper has been typeset from a \LaTeX file prepared by the author.